TWO-PORT POLARIZATION INDEPENDENT ELECTRO-OPTICALLY TUNABLE WAVELENGTH FILTER IN LITHIUM NIOBATE

A Thesis

by

YANG PING

Submitted to the Office of Graduate Studies of
Texas A&M University
in partial fulfillment of the requirements for the degree of

MASTER OF SCIENCE

August 2003

Major Subject: Electrical Engineering

TWO-PORT POLARIZATION INDEPENDENT ELECTRO-OPTICALLY TUNABLE WAVELENGTH FILTER IN LITHIUM NIOBATE

A Thesis

by

YANG PING

Submitted to Texas A&M University
in partial fulfillment of the requirements
for the degree of

MASTER OF SCIENCE

Approved as to style and content by:

Ohannes Eknoyan (Chair of Committee)	Henry F. Taylor (Member)
Andrew K. Chan (Member)	Lihong Wang (Member)
Chanan Singh (Head of Department)	

August 2003

Major Subject: Electrical Engineering

ABSTRACT

Two-port Polarization Independent Electro-Optically Tunable Wavelength Filter in Lithium Niobate. (August 2003)

Yang Ping, B.S., Tsinghua University

Chair of Advisory Committee: Dr. Ohannes Eknoyan

Two-port polarization independent electro-optically wavelength tunable filters based on asymmetric Mach-Zehnder structure in $LiNbO_3$ substrate have been developed for 1.55μm application. The operation principle is based on Mach-Zehnder interference and TE↔TM mode conversion. Fabrication parameters for channel waveguides, interferometers and mode converters have been optimized. 7μm wide single mode straight channel waveguides were produced by diffusing 1050-1100Å thick Ti into $LiNbO_3$ substrate. Insertion loss of 3.6dB was achieved for both TE and TM polarization. Mach-Zehnder interferometer performance was optimized by testing the Y-branch on samples cut in half length compared to complete device. Best results were obtained from samples that were produced by diffusion at 1025°C for 11 hours of 1050Å thick Ti film, and by diffusion at 1025°C for 12 hours of 1090Å thick Ti film. Metal electrodes were added to one arm of asymmetric Mach-Zehnder interferometers to evaluate electro-optic modulation. Modulation depth as high as 99.6% for TE mode and 98.9% for TM mode

were obtained. TE↔TM mode conversion was demonstrated on straight channel waveguides with conversion efficiency greater than 96% utilizing 500 strain inducing SiO_2 grating pads with 21μm spatial period. Two-port polarization independent electro-optically tunable wavelength filters were produced based on the optimized parameters described above. The –3dB bandwidth of the filter is 2.4nm. The nearest side lobe to the main peak is more than 13dB below the central lobe for both TE polarization and TM polarization. A thermal tuning rate of –0.765nm/°C is obtained. An electrical tuning range of 12.8nm and a tuning rate of 0.08nm/V were achieved.

To My Parents

ACKNOWLEDGMENTS

I would like to express my gratitude to all those who helped me complete this thesis. I want to thank Dr. O. Eknoyan for serving as my committee chair and for his stimulating suggestions and encouragement during these past years. I would also like to thank Dr. H. F. Taylor for providing advice and help in addition to being one of my committee members. Thanks to Dr. A. K. Chan and Dr. L. Wang for also serving on my committee and helping on my thesis.

I am grateful to Mr. R. A. Atkins, our lab manager, for his technical training and support in my research. Without his help, this thesis could never have been finished.

And needless to say, I am grateful to all of my friends and colleagues, P. Tang, D. Gu, R. Wang, A. Bhatranand, N. Supharan, H. Kuo, R.H. Kim, Z. Xie, Y. Chen and Y. W. Shin, for their friendship and help.

I would like to give my special thanks to Bin for being with me every single moment. And finally I thank my parents and my sister, for their love and encouragement.

TABLE OF CONTENTS

TABLE OF CONTENTS (Continued)

TABLE OF CONTENTS (Continued)

Page

LIST OF FIGURES

LIST OF FIGURES (Continued)

LIST OF FIGURES (Continued)

LIST OF TABLES

CHAPTER I

INTRODUCTION

A communication system transmits information from one place to another. Information is often carried by an electromagnetic carrier wave whose frequency can vary from a few megahertz to several hundred terahertz. Optical communication systems use high carrier frequencies (~100 THz) in the visible or near-infrared region of the electromagnetic spectrum. They are often called lightwave systems to distinguish them from the microwave systems, whose carrier frequency is much lower (~1GHz). Fiber optic communication systems are lightwave systems that employ optical fibers for information transmission [1]. Such systems are now deployed world wide and it has become a major carrier of information, especially for long distance telephone systems and data-intensive computer networks. Optical communication systems are superior to conventional electrical wire communication systems in the following aspects:

- huge bandwidth,
- low signal attenuation (as low as 0.2 dB/km),
- low signal distortion,
- low power requirement,

This thesis follows the style and format of *IEEE Journal of Lightwave Technology.*

- light weight material usage (optical fiber),
- small space requirement, and
- low cost.

In optical communication, wavelength-division multiplexing (WDM) is an approach that can exploit the available huge optical bandwidth. And the tunable optical filter is a key component in WDM systems for its potential use at the receiver ends for channel selection. A number of optical filter approaches have been proposed and developed [2]. Based on the mechanisms of wavelength filtering, they can be grouped into three categories as the following:

- Filters that are based on the wavelength dependence of interferometric phenomena, such as Fabry-Perot filters and Mach-Zehnder filters.
- Filters that are based on the wavelength dependence of coupling between orthogonal polarizations of optical fields induced by external perturbations, such as acousto-optic and electro-optic filters.
- Filters that are based on semiconductor resonant structures [2]. Such devices are capable of providing gain as well as wavelength selectivity but are not the topic of this research.

Of these technologies, only electro-optic tunable filter (EOTF) [3, 4] can be tuned in

sub-microsecond time periods, which is needed for fast packet-switched networks [5] and provide a relatively large tuning rate as well. EOTFs can be realized in ferroelectric birefringent materials like lithium niobate ($LiNbO_3$), which has been researched at Texas A&M University for many years. Tuning is accomplished by changing the refractive index of the waveguide through the Pockels effect, where the change of the refractive index of the guiding optical medium is linearly proportional to an applied electrical field which is imposed through an external voltage.

The primary purpose of this research is to develop a new polarization-independent electro-optically tunable filter in $LiNbO_3$, which can be used at the front end of a direct detection receiver.

A brief theoretical review is given in Chapter II. An analysis of the electro-optically tunable filter is presented in Chapter III. Device fabrication is described in Chapter IV. Experimental results are discussed in Chapter V. Finally, conclusion results are summarized in Chapter VI.

CHAPTER II

THEORETICAL REVIEW

In this chapter, a brief review of wave propagation properties and optical waveguides based on Maxwell's Equations is given. Optical indicatrix in uniaxial crystals is discussed and electro-optic effect is explained. Coupled mode theory is presented to describe TE↔TM mode conversion.

A. Wave Propagation

Optical propagation inside a dielectric crystal is mainly a wave phenomenon. The governing equations for electromagnetic wave propagation are Maxwell's Equations:

$$\nabla \times \mathbf{E} = -\mu_0 \frac{\partial \mathbf{B}}{\partial t} \tag{1}$$

$$\nabla \times \mathbf{H} = \mathbf{J} + \frac{\partial \mathbf{D}}{\partial t} \tag{2}$$

$$\nabla \cdot \mathbf{D} = \rho \tag{3}$$

$$\nabla \cdot \mathbf{B} = 0 \tag{4}$$

and

$$\mathbf{D} = \varepsilon_0 \mathbf{E} + \mathbf{P} = \varepsilon \mathbf{E} \tag{5}$$

$$\mathbf{B} = \mu_0 (\mathbf{H} + \mathbf{M}) = \mu \mathbf{H} \tag{6}$$

where **E** and **H** represent electric and magnetic field vectors, **D** and **B** are the electric and magnetic displacement vectors, **J** and ρ are current and charge densities, ε_0 and μ_0 are the

permittivity and permeability of free space, **P** and **M** are the electric and magnetic polarization of the medium, receptively. For source free homogeneous dielectric medium, **J** and ρ are zero, μ is usually a constant, and ε is a diagonal matrix if a proper coordinate system is chosen,

$$\varepsilon = \begin{pmatrix} \varepsilon_1 & 0 & 0 \\ 0 & \varepsilon_2 & 0 \\ 0 & 0 & \varepsilon_3 \end{pmatrix}. \tag{7}$$

Taking the curl of both sides of equation (1), substituting **B** with equation (6), using $\nabla \times \nabla \times \mathbf{E} = \nabla(\nabla \cdot \mathrm{E}) - \nabla^2 \mathbf{E}$ and equations (2), (3), (5), yields

$$\nabla^2 \mathbf{E} - \varepsilon \mu_0 \frac{\partial^2 \mathbf{E}}{\partial t^2} = 0. \tag{8}$$

For a monochromatic wave with angular frequency ω, the electric field **E** should take the form:

$$\mathbf{E}(\mathbf{r}, t) = \mathbf{E}(\mathbf{r}) e^{-i\omega t}. \tag{9}$$

Equation (8) can be rewritten using equation (9) as

$$\nabla^2 \mathbf{E}(\mathbf{r}) + k_0^2 n^2 \mathbf{E}(\mathbf{r}) = 0 \tag{10}$$

where $k_0 = \omega / c$ is the propagation constant in free space and $n = \sqrt{\varepsilon_r \mu_r}$ is the refractive index of the material.

B. Optical Waveguides

An optical waveguide is generally a thin high refractive index layer surrounded by lower refractive index materials. A simple case is the step-index infinite planar slab waveguide in dielectric materials, which is depicted in Fig. 1.

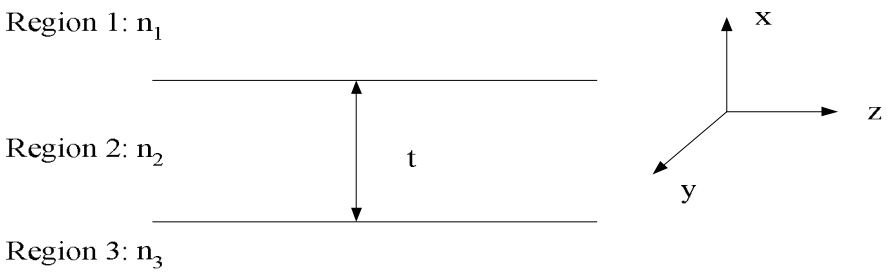

Fig. 1. Planar dielectric waveguide structure.

A mode of such a waveguide at a given frequency is described by a solution of equation (10). The solutions are subject to the electromagnetic boundary conditions at the interface between two dielectrics [6]:

$$\begin{aligned} E_{1t} &= E_{2t} \\ H_{1t} &= H_{2t} \\ D_{1n} &= D_{2n} \\ B_{1n} &= B_{2n}. \end{aligned} \tag{11}$$

Consider the case of z-propagation wave with propagation constant β and no y variation, which is shown in Fig. 1, and applying equation (11) to equation (10) and the waveguide structure, yields [7]

$$\text{Region 1: } \frac{\partial^2}{\partial x}E(x)+[k_0{}^2n_1{}^2-\beta^2]E(x)=0$$
$$\text{Region 2: } \frac{\partial^2}{\partial x}E(x)+[k_0{}^2n_2{}^2-\beta^2]E(x)=0 \qquad (12)$$
$$\text{Region 3: } \frac{\partial^2}{\partial x}E(x)+[k_0{}^2n_3{}^2-\beta^2]E(x)=0$$

where E(x) is either an x- or y- component of E(x).

Assuming $n_2>n_3>n_1$, the characteristics of waveguide modes can be analyzed by considering various β values. In the range of $\beta<k_0n_1$, the solution of E(x) is sinusoidal in all the three regions. This is called radiation mode and the wave is therefore not guided.

For $k_0n_1<\beta<k_0n_3$, solutions in region 2 and 3 are sinusoidal and are exponentially decaying in region1. This is commonly referred to as substrate radiation modes.

When $k_0n_3<\beta< k_0n_2$, the solution is sinusoidal in region 2 and exponential in region 1 and 3, making it possible to have a bounded solution for E(x) in the middle region that satisfies the boundary conditions and decays in the outer regions. The optical wave in this case is confined to the middle layer and its vicinity. Thus, these are guided modes.

The final case, $\beta>k_0n_2$, yields a solution where the field distribution increases exponentially away from the waveguide, which is not realizable.

The optical field distributions of all above cases are illustrated in Fig. 2.

From the above discussion, it is clear that the condition for the existence of a guided mode in a planar slab dielectric waveguide with $n_2>n_3>n_1$ is

$$k_0n_3<\beta< k_0n_2. \qquad (13)$$

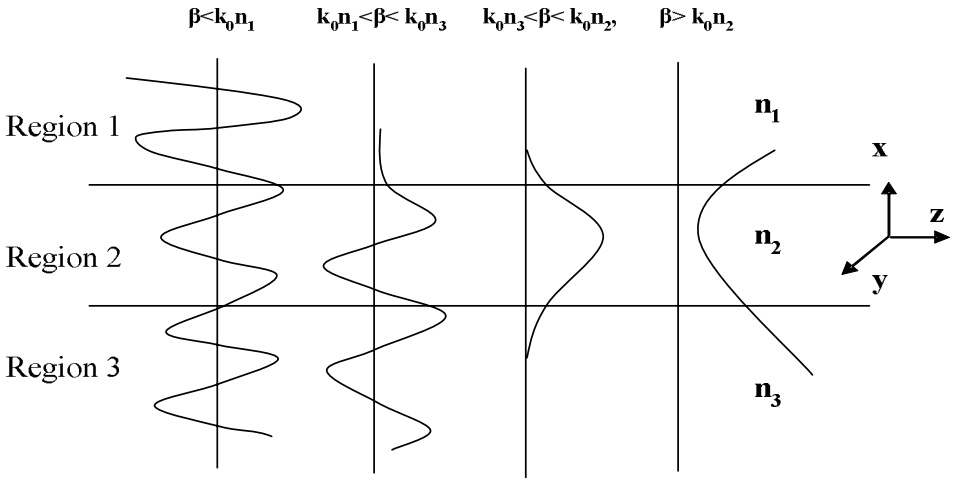

Fig. 2. The electrical field distributions corresponding to different values of β in a three-layer waveguide with $n_2>n_3>n_1$.

This also implies that confined modes are possible only when $n_2>n_3, n_1$, that is, the inner layer has a large refractive index than that of outside layers.

The waveguide structure shown in Fig. 1 can generally support a finite number of guided modes, which can be further divided into two groups based on the polarization directions. One is called transverse electric (TE) mode, the other is called transverse magnetic (TM) mode. When a plane wave with TE or TM polarization is incident on the dielectric core-cladding interface, the reflected and transmitted waves maintain the TE or TM polarization. Therefore, there is no mixing between TE or TM components in the propagation. The field components for the TE and TM modes of the slab waveguide are summarized in Table 1 [8].

Table 1. Summary of field components for slab waveguides
($\phi(x)$ stands for E_y in TE modes or H_y in TM mode).

TE Modes	TM Modes
$E_z = 0$	$H_z = 0$
$E_x = 0$	$H_x = 0$
$H_y = 0$	$E_y = 0$
$E_y = \phi(x)$	$H_y = \phi(x)$
$H_x = -\frac{\beta}{k}\sqrt{\frac{\varepsilon_0}{\mu_0}}\varphi(x)$	$E_x = \frac{\beta}{k}\frac{1}{n^2}\sqrt{\frac{\mu_0}{\varepsilon_0}}\varphi(x)$
$H_z = -\frac{i}{k}\sqrt{\frac{\varepsilon_0}{\mu_0}}\varphi'(x)$	$E_z = \frac{i}{k}\frac{1}{n^2}\sqrt{\frac{\mu_0}{\varepsilon_0}}\varphi'(x)$

C. Optical Indicatrix in Uniaxial Crystals and Electro-Optic Effect

The refractive index n defined in section **A** is usually a constant for isotropic materials, but it is direction and polarization dependent for anisotropic materials due to the fact that ε is a 3×3 matrix. The refractive index for a specific direction and polarization in an anisotropic material can be derived from the following equation [9]

$$\frac{x^2}{n_x^2}+\frac{y^2}{n_y^2}+\frac{z^2}{n_z^2}=1 \tag{14}$$

where x, y and z are the principal dielectric axes, that is, the directions in the crystal along which **D** and **E** are parallel. n_x, n_y and n_z are the refractive indexes along x, y and z

axis respectively. In uniaxial crystals, such as $LiNbO_3$ and $LiTaO_3$, $n_x=n_y=n_o$ and $n_z=n_e$, equation (14) can be simplified as

$$\frac{x^2}{n_o^2}+\frac{y^2}{n_o^2}+\frac{z^2}{n_e^2}=1 \tag{15}$$

where the index ellipsoid is rotary symmetrical with respect to the z axis, which is also called the optic axis.

Fig. 3 illustrates the wave propagation in a uniaxial crystal. The direction of propagation is along **k**. Because of the circular symmetry about z axis, one can choose the y axis to coincide with the projection of **k** vector on the x-y plane without loss of generality. The intersection ellipse of the plane normal to **k** with the ellipsoid is shaded in the Fig. 3. The two polarization eigen states of **D** are parallel to the major and minor axes of the ellipse, and are said to be extraordinary wave (D_e) and ordinary wave (D_o),

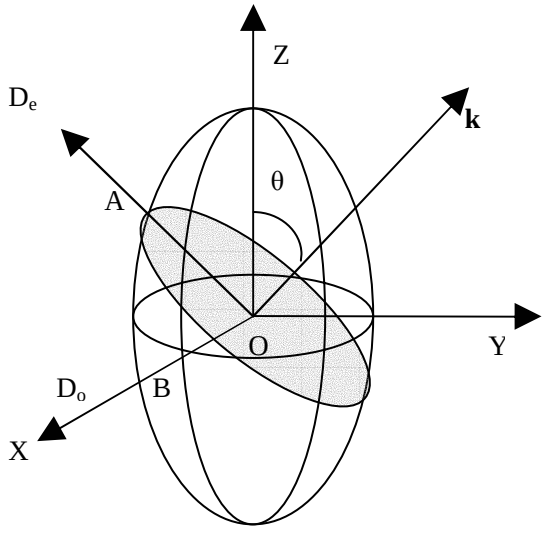

Fig. 3. Index ellipsoid of uniaxial crystals.

respectively. The length of the semi-major axis OA equals to the refractive index $n_e(\theta)$ for extraordinary wave, whereas OB which equals n_o is the one for the ordinary wave. Fig. 3 also indicates that the polarization direction and the refractive index of ordinary wave remain unchanged with respect to change of θ, which is the angle between the optic axis and the propagation direction **k**, while those of the extraordinary wave are dependent on θ.

The index of extraordinary wave is equal to OA in the Fig. 3, and is given by

$$\frac{1}{n_e^2(\theta)} = \frac{\sin^2(\theta)}{n_e^2} + \frac{\cos^2(\theta)}{n_o^2}. \tag{16}$$

In section **B** it was stated that, given a direction in a crystal, there in general exist two possible linearly polarized modes (TE and TM). Each mode possesses a unique polarization direction and a corresponding index of refraction (i.e., a velocity of propagation) [9], which can be easily found through equation (14).

The linear electro-optic (Pockels) effect, which is the basis for active waveguide device control, provides a change in refractive index proportional to the applied electric field [10]. The effect of an electric field on the propagation is expressed most conveniently by giving the changes in the constants $1/n_x^2$, $1/n_y^2$, $1/n_z^2$ of the index ellipsoid. The equation of the index ellipsoid in the presence of an electric field is expressed as [9]

$$\left(\frac{1}{n^2}\right)_1 x^2 + \left(\frac{1}{n^2}\right)_2 y^2 + \left(\frac{1}{n^2}\right)_3 z^2 + \left(\frac{1}{n^2}\right)_4 yz + \left(\frac{1}{n^2}\right)_5 xz + \left(\frac{1}{n^2}\right)_6 xy = 1. \tag{17}$$

With zero applied electric field, equation (17) reduces to (14), i.e.

$$\left(\frac{1}{n^2}\right)_1\Big|_{E=0}=\frac{1}{n_x^2},\ \left(\frac{1}{n^2}\right)_2\Big|_{E=0}=\frac{1}{n_y^2},\left(\frac{1}{n^2}\right)_3\Big|_{E=0}=\frac{1}{n_z^2},$$

$$\left(\frac{1}{n^2}\right)_4\Big|_{E=0}=\left(\frac{1}{n^2}\right)_5\Big|_{E=0}=\left(\frac{1}{n^2}\right)_6\Big|_{E=0}=0.$$

The linear change in the coefficients of the index ellipsoid due to an applied electric field (E_j) along the principle crystal axis is defined by

$$\Delta\left(\frac{1}{n^2}\right)_i=\sum_{j=1}^{3}r_{ij}E_j, \tag{18}$$

where i=1,2,…,6 and r_{ij} is a 6×3 electro-optic tensor.

In $LiNbO_3$, $n_x=n_y=n_o$ and $n_z=n_e$ in equation (14) and the electro-optic tensor is [11]

$$\begin{bmatrix}0 & -r_{22} & r_{13}\\ 0 & r_{22} & r_{13}\\ 0 & 0 & r_{33}\\ 0 & r_{51} & 0\\ r_{51} & 0 & 0\\ -r_{22} & 0 & 0\end{bmatrix}. \tag{19}$$

If only a z-directed electric field E_z exists in the $LiNbO_3$ crystal, the modified refractive index become

$$\frac{1}{n_{x'}^2}=\frac{1}{n_o^2}+r_{13}E_z. \tag{20}$$

For $LiNbO_3$, $r_{13}=8.6\times10^{-12}\ {}^{m}\!/_{V}$, $r_{33}=30.8\times10^{-12}\ {}^{m}\!/_{V}$, n_o=2.29, n_e=2.20 (for λ=1.4μm, at 24.5 °C) [12]. Assuming $r_{13}E_z \ll n_o^{-2}$ and $r_{33}E_z \ll n_e^{-2}$, using the differential relation

$$dn = -\left(\frac{n^3}{2}\right) d\left(\frac{1}{n^2}\right),$$

yields

$$n_{x'} = n_o - \frac{n_o^3}{2} r_{13} E_z, \tag{21}$$

and similarly,

$$n_{y'} = n_o - \frac{n_o^3}{2} r_{13} E_z, \tag{22}$$

$$n_{z'} = n_e - \frac{n_e^3}{2} r_{33} E_z. \tag{23}$$

D. TE↔TM Mode Conversion

In optical waveguide without perturbation, modes satisfy the wave equation (8). Due to refractive index perturbation, a TE polarized optical wave may convert to a TM polarized optical wave and vice versa. A large number of devices exploit the coupling between such modes. The basic characteristics of TE↔TM mode conversion can be described using small perturbation of the dielectric medium polarization vector **P**, and examining its effect on the time dependent wave equation [13]. Below is the wave equation in a dielectric medium

$$\nabla^2 \mathbf{E}(\mathbf{r}, t) = \mu\varepsilon(r) \frac{\partial^2 \mathbf{E}(\mathbf{r}, t)}{\partial t^2}. \tag{24}$$

Using equation (5), (24) yields the following

$$\nabla^2 \mathbf{E}(\mathbf{r},t) = \mu\varepsilon_0 \frac{\partial^2 \mathbf{E}(\mathbf{r},t)}{\partial t^2} + \mu \frac{\partial^2 \mathbf{P}(\mathbf{r},t)}{\partial t^2}. \tag{25}$$

The total medium polarization can be taken as the sum

$$\mathbf{P}(\mathbf{r},t) = \mathbf{P}_0(\mathbf{r},t) + \mathbf{P}_{\text{pert}}(\mathbf{r},t) \tag{26}$$

where

$$\mathbf{P}_0(\mathbf{r},t) = [\varepsilon(\mathbf{r}) - \varepsilon_0]\mathbf{E}(\mathbf{r},t) \tag{27}$$

is the polarization induced by $\mathbf{E(r},t)$ in the unperturbed waveguide whose dielectric constant is $\varepsilon\mathbf{(r)}$. Using equation (26) and (27), equation (25) gives

$$\nabla^2 \mathrm{E}_i(\mathbf{r},t) - \mu\varepsilon(\mathbf{r}) \frac{\partial^2 \mathrm{E}_i(\mathbf{r},t)}{\partial t^2} = \mu \frac{\partial^2}{\partial t^2}[\mathbf{P}_{\text{pert}}(\mathbf{r},t)]_i \tag{28}$$

where i represents either x, y or z.

In the case of x-cut y-propagation waveguide as shown in Fig. 4, TE polarized mode has transverse electrical field distribution in the z direction while TM mode has transverse electrical field distribution in the x direction. From equation (28), a z-directed

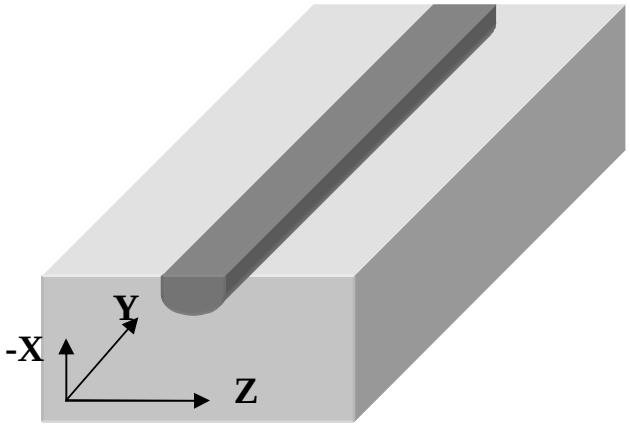

Fig. 4. A x-cut y-propagation Ti:$LiNbO_3$ waveguide.

perturbation induced medium polarization (P_z) is required for TM→TE coupling, and an x-directed perturbation induced medium polarization (P_x) is needed to achieve TE→TM coupling. In order to produce TE↔TM mode conversion, both of these conditions should be fulfilled.

Considering the z component of equation (5) only, it yields

$$D_3 = \sum_{j=1}^{3} \varepsilon_{3j} E_j = \varepsilon_0 E_3 + P_3, \tag{29}$$

or:

$$P_3 = \sum_{j=1}^{3} \varepsilon_{3j} E_j - \varepsilon_0 E_3. \tag{30}$$

Thus the perturbation $[\mathbf{P}_{pert}]_z$ is

$$[\mathbf{P}_{pert}]_z = \Delta P_3 = \sum_{j=1}^{3} \Delta\varepsilon_{3j} E_j. \tag{31}$$

Assuming E_z=0 and E_y is negligible (TM), equation (31) reduces to

$$\Delta P_3 = \Delta\varepsilon_{31} E_1. \tag{32}$$

Using the following identity

$$\left[\frac{1}{n^2}\right]_{31} = \left[\frac{1}{n^2}\right]_5 = -\frac{\varepsilon_0 \varepsilon_{31}}{\varepsilon_{33}\varepsilon_{11}}, \tag{33}$$

gives

$$\Delta P_3 = \Delta\varepsilon_{31} E_1 = -\frac{\varepsilon_{33}\varepsilon_{11}}{\varepsilon_0} \Delta\left(\frac{1}{n^2}\right)_5 E_1. \tag{34}$$

Equation (34) relates a z directed medium polarization to an x directed optical electric field through the index change of n_5. Similarly, for a TE-polarized optical wave, the change of medium polarization component P_1 can be expressed as

$$\Delta P_1 = \Delta\varepsilon_{13} E_3 = -\frac{\varepsilon_{33}\varepsilon_{11}}{\varepsilon_0}\Delta\left(\frac{1}{n^2}\right)_5 E_3. \tag{35}$$

The TE↔TM mode conversion can be described by [7]

$$\begin{aligned}\frac{dA_m}{dz} &= -i\kappa_m B_m e^{-i(\beta_m^{TM}-\beta_m^{TE})y}\\ \frac{dB_m}{dz} &= -i\kappa_m A_m e^{-i(\beta_m^{TM}-\beta_m^{TE})y}\end{aligned} \tag{36}$$

where A_m and B_m are the amplitudes of TE and TM m^{th} mode; β_m^{TE} and β_m^{TM} are the propagation constants of TE and TM m^{th} mode; κ is the coupling coefficient; y is the direction of propagation.

The solution to equation (36), subject to boundary conditions $B_m(0)=B_0$ and $A_m(0)=0$, is

$$\begin{aligned}B(y) &= B_0 e^{i\delta y}\{\cos[(\kappa^2+\delta^2)^{1/2} y] - i\frac{\delta}{(\kappa^2+\delta^2)^{1/2}}\sin[(\kappa^2+\delta^2)^{1/2} y]\}\\ A(y) &= -iB_0 e^{-i\delta y}\frac{\kappa}{(\kappa^2+\delta^2)^{1/2}}\sin[(\kappa^2+\delta^2)^{1/2} y]\end{aligned} \tag{37}$$

where $\delta \equiv \frac{(\beta_m^{TM}-\beta_m^{TE})}{2}$ is the phase mismatch factor. A plot of the mode power variation with position along the propagation direction for the phase-matched (δ=0) and δ≠0 cases are shown in Fig. 5.

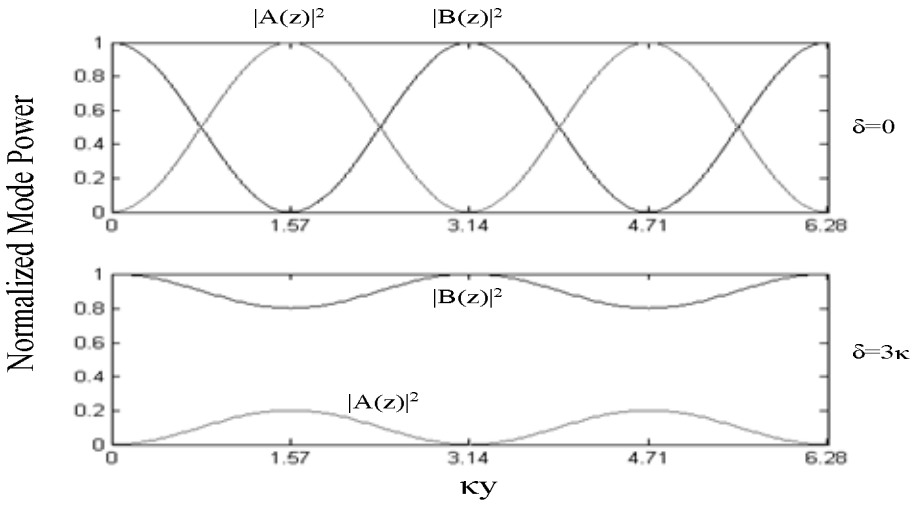

Fig. 5. Power exchange between TE and TM modes.

It is obvious from Fig. 5 that the conversion is most efficient when the phase match condition ($\delta=0$) is fulfilled. A deliberate off-diagonal index change with period [13]

$$\Lambda = \frac{2\pi}{\left|\beta_m^{TM} - \beta_m^{TE}\right|} = \frac{2\pi}{\left|\frac{2\pi \cdot n_{TM}}{\lambda_0} - \frac{2\pi \cdot n_{TE}}{\lambda_0}\right|} = \frac{\lambda_0}{\left|n_{TM} - n_{TE}\right|} = \frac{\lambda_0}{\Delta n} \tag{38}$$

can be used to neutralize the phase mismatch if it is not naturally matched, where Λ is the period of perturbation, λ_0 is the wavelength in free space, n_{TM} and n_{TE} are the refractive indices for TM and TE modes. The phase match condition causes the mode conversion to be wavelength selective and allow wavelength tuning by changing the birefringence Δn.

CHAPTER III

DEVICE ANALYSIS

In this chapter, the structure of the tunable optical filter is presented and its special features are discussed. The operation principle of the device is also explained.

The basic structure of the integrated electro-optically wavelength tunable filter is illustrated in Fig. 6.

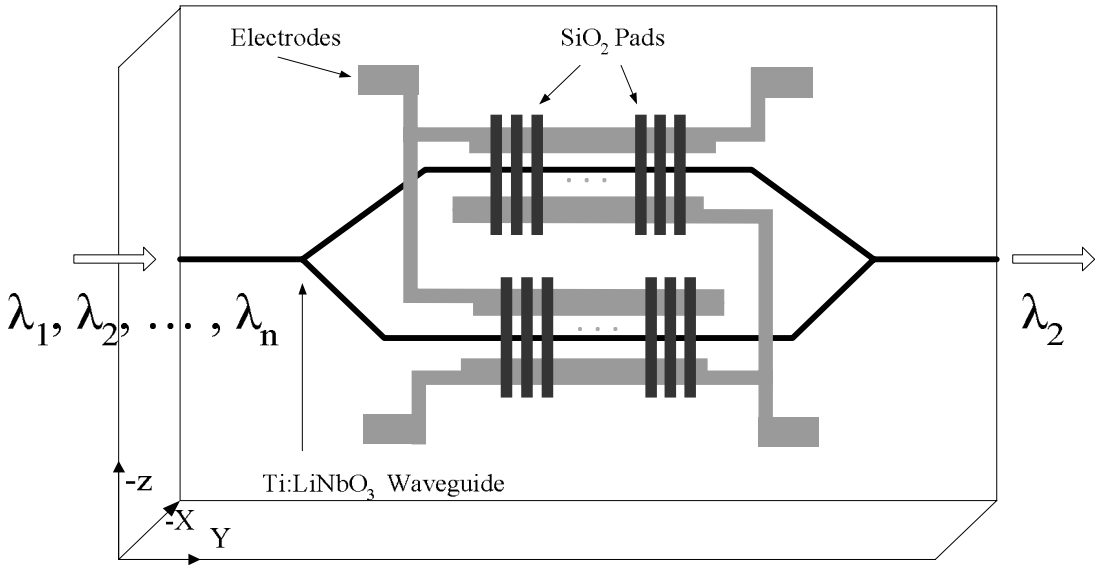

Fig. 6. Schematic diagram of filter structure.

It consists of a 3-dB beam splitter at the Y-branch near the input side, a beam combiner at the Y-branch near the output side, one pair of electrodes and two static strain-induced phase-matched polarization mode converters in the upper and lower waveguide arms between the splitter and combiner. It differs from conventional designs in the following

respects:

- It has an asymmetric Mach-Zehnder interferometer configuration, which introduces a half-wavelength optical path difference for the waveguide arms between the two branching points.
- The relative positions of the polarization coupling regions in the two waveguide arms are displaced in the propagation direction by half of the spatial period of the perturbation responsible for polarization coupling [3].
- This device has one-input port and one-output port and it allows only a wavelength that satisfies the phase match condition of the polarization converters to emerge from the output port.

To analyze this filter design, consider an incoming wavelength multiplexed optical signal consisting of λ_1, $\lambda_2 \ldots \lambda_n$ incident on a single mode optical waveguide at the input port as shown in Fig. 6. For simplicity, assume the incident light is polarized in TE mode. At the first Y-branch, the signal splits into two parts by the beam splitter and is directed toward the upper and the lower mode converter regions. At the output of each mode converter, the original state of the polarization converts to its orthogonal mode, in this case TM, only at one wavelength, say λ_2, which is phase-matched with the static strain grating period. The converted polarization at λ_2 and unconverted polarization at all other λs then proceed toward the recombiner at the second Y-branch which is identical in

design to the splitter at the first Y-branch. Because of the combination of half-wavelength in optical path length between the upper and lower arms, and also the half spatial period displacement in the regions of periodic perturbation responsible for coupling in each arm, only fields for the converted wavelength λ_2 arrive in phase allowing them to recombine and exit via the output port. On the other hand, the fields for all other λs arrive out of phase and radiate into the substrate. Wavelength tuning can be accomplished by an applied voltage through the surface electrodes, which changes the birefringence in the waveguide arms and hence the wavelength for which the phase matching condition is satisfied.

The specific explanation of the device's operating principal is presented in the following [14]. The detailed filter configuration is presented in Fig. 7.

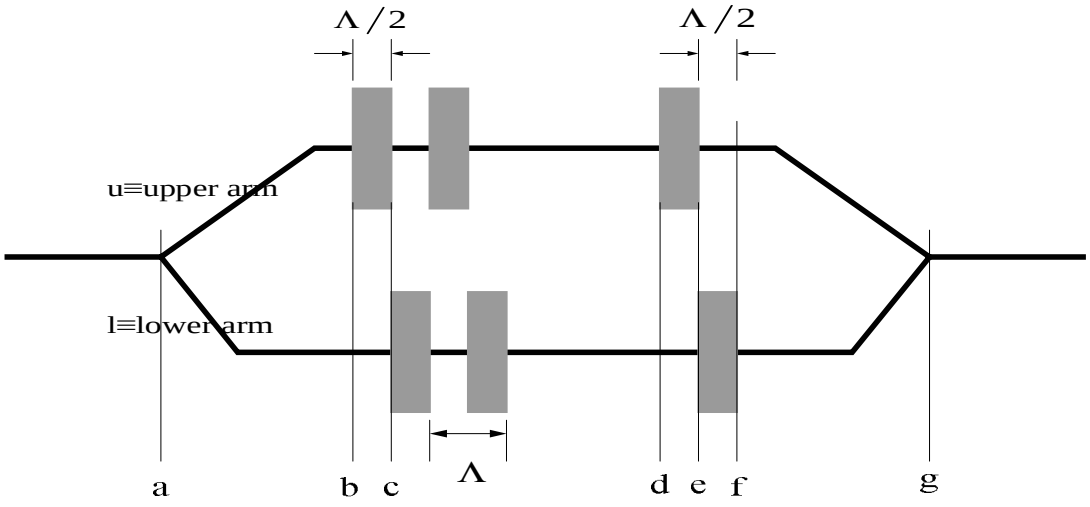

Fig. 7. Interferometer structure.

In Fig. 7, the shaded parts represent the SiO_2 grating pads and Λ is the spatial period of the perturbation. The optical path length difference from point "a" to "g" between the upper and lower arm, with upper arm longer, is $\frac{\lambda}{2}$, i.e.

$$L_{ag}^{u} - L_{ag}^{l} = \frac{\lambda}{2}.$$

Due to symmetry, the path difference from "a" to "b" between upper and lower arms is $\frac{\lambda}{4}$, i.e.

$$L_{ab}^{u} - L_{ab}^{l} = \frac{\lambda}{4} \Rightarrow L_{ab}^{u} = L_{ab}^{l} + \frac{\lambda}{4}.$$

Assuming 3-dB splitter, which divides the power equally, then the electric fields for the lightwave are:

at point "b":

In the lower arm is

$$\mathbf{E}_{l\ (z=b)}^{w} = \frac{E_0}{\sqrt{2}} e^{-i\beta L_{ab}^{l}}, \tag{39}$$

and in the upper arm is

$$\mathbf{E}_{l\ (z=b)}^{w} = \frac{E_0}{\sqrt{2}} e^{-i\beta L_{ab}^{u}} = \frac{E_0}{\sqrt{2}} e^{-i\beta (L_{ab}^{l} + \frac{\lambda}{4})} = \frac{E_0}{\sqrt{2}} e^{-i(\beta L_{ab}^{l} + \frac{\pi}{2})},\ (\beta = \frac{2\pi}{\lambda}) \tag{40}$$

i.e. light at upper arm accumulates an additional phase of $\frac{\pi}{2}$ relative to lower arm. The superscript "w" indicates optical wave.

Let us consider TE polarized input for the time being, then $\beta = \beta_{TE} = \frac{2\pi}{\lambda} n_{TE}$ and let

$$\beta_{TE} L_{ab}^{l} = \frac{2\pi}{\lambda_0} n_{TE} L_{ab}^{l} \equiv \phi_{ab}^{TE}.$$

Hence

$$\mathbf{E}^{w}_{l\ (z=b)} = \frac{E_0}{\sqrt{2}} e^{-i\varphi^{TE}_{ab}}$$
$$\mathbf{E}^{w}_{u\ (z=b)} = \frac{E_0}{\sqrt{2}} e^{-i(\varphi^{TE}_{ab}+\frac{\pi}{2})}. \quad (41)$$

at point "e" in the upper arm:

Assuming phase match condition is satisfied at wavelength λ_0, light emerging at "e" in upper arm fully converts to TM mode and acquires an additional phase of $\frac{\pi}{2}$ over its normal accumulated phase in the conversion region within length L_0. Thus,

$$\mathbf{E}^{w}_{u\ (z=e)} = \mathbf{E}^{w}_{u\ (z=b)} \cdot e^{-i(\beta_{TE}L_0+\frac{\pi}{2})}$$
$$= \frac{E_0}{\sqrt{2}} e^{-i(\varphi^{TE}_{ab}+\frac{\pi}{2}+\beta_{TE}L_0+\frac{\pi}{2})}. \quad (42)$$

at point "f" in the upper arm:

From "e" to "f", the propagating lightwave (now TM mode) accumulates a phase $\phi^{TM}_{ef} = \beta_{TM}L_{ef} = \beta_{TM}\frac{\Lambda}{2}$ with $\beta_{TM} = \frac{2\pi}{\lambda}n_{TM}$. Thus,

$$\mathbf{E}^{w}_{u\ (z=f)} = \mathbf{E}^{w}_{u\ (z=e)} \cdot e^{-i\beta_{TM}\frac{\Lambda}{2}}$$
$$= \frac{E_0}{\sqrt{2}} e^{-i(\phi^{TE}_{ab}+\frac{\pi}{2}+\beta_{TE}L_0+\frac{\pi}{2}+\beta_{TM}\frac{\Lambda}{2})}. \quad (43)$$

at point "c" in the lower arm:

The light maintains TE mode from "b" to "c" and acquires a phase of $\phi^{TE}_{bc} = \beta_{TE}L_{bc} = \beta_{TE}\frac{\Lambda}{2}$. Hence,

$$\begin{aligned}\mathbf{E}_{l\ (z=c)}^{w} &= \mathbf{E}_{l\ (z=b)}^{w}\cdot e^{-i\beta_{TE}\frac{\Lambda}{2}} \\ &= \frac{E_0}{\sqrt{2}} e^{-i(\phi_{ab}^{TE}+\beta_{TE}\frac{\Lambda}{2})}.\end{aligned} \tag{44}$$

at point "f" in the lower arm:

Under previous assumption phase match condition is satisfied at λ, then light at point "f" in the lower arm fully converts to TM mode and acquires an additional phase of $\frac{\pi}{2}$ over its normal accumulated phase in the conversion region within length L_0, i.e.

$$\begin{aligned}\mathbf{E}_{l\ (z=f)}^{w} &= \mathbf{E}_{l\ (z=c)}^{w}\cdot e^{-i(\beta_{TE}L_0+\frac{\pi}{2})} \\ &= \frac{E_0}{\sqrt{2}} e^{-i(\phi_{ab}^{TE}+\beta_{TE}\frac{\Lambda}{2}+\beta_{TE}L_0+\frac{\pi}{2})}.\end{aligned} \tag{45}$$

at point "g"(final):

Again, due to symmetry, there is $\frac{\lambda}{4}$ phase difference between upper and lower arm from point "f" to "g", with upper arm longer. We have:

in lower arm,

$$\phi_{fg}^{l} = \beta_{TM}\cdot L_{fg} \equiv \phi_{fg}^{TM};$$

and in upper arm,

$$\phi_{fg}^{u} = \beta_{TM}\cdot(L_{fg}+\frac{\lambda}{4}) = \beta_{TM}L_{fg}+\frac{2\pi}{\lambda}\cdot\frac{\lambda}{4} \equiv \phi_{fg}^{TM}+\frac{\pi}{2}. \tag{46}$$

Also in the tapered section at output, 2 modes (symmetric and asymmetric) are excited, i.e. intensity from each arm drops by $\frac{1}{2}$, therefore E^w drops by another $\frac{1}{\sqrt{2}}$ factor. Thus,

$$\begin{aligned}\mathbf{E}^{w}_{u\,(z=g)} &= \mathbf{E}^{w}_{u\,(z=f)} \cdot e^{-i(\phi^{TM}_{fg}+\frac{\pi}{2})} \\ &= \frac{E_0}{\sqrt{2}} e^{-i(\phi^{TE}_{ab}+\frac{\pi}{2}+\beta_{TE}L_0+\frac{\pi}{2}+\beta_{TM}\frac{\Lambda}{2}+\phi^{TM}_{fg}+\frac{\pi}{2})} \cdot \frac{1}{\sqrt{2}}\end{aligned} \tag{47}$$

and

$$\begin{aligned}\mathbf{E}^{w}_{l\,(z=g)} &= \mathbf{E}^{w}_{l\,(z=f)} \cdot e^{-i\phi^{TM}_{fg}} \\ &= \frac{E_0}{\sqrt{2}} e^{-i(\phi^{TE}_{ab}+\beta_{TE}\frac{\Lambda}{2}+\beta_{TE}L_0+\frac{\pi}{2}+\phi^{TM}_{fg})} \cdot \frac{1}{\sqrt{2}}.\end{aligned} \tag{48}$$

The total electrical field at the output is

$$\mathbf{E}^{w}_{out} = \mathbf{E}^{w}_{u\,(z=g)} + \mathbf{E}^{w}_{l\,(z=g)}, \tag{49}$$

and the output light intensity can be expressed as

$$I_{out} = \left|\mathbf{E}^{w}_{out}\right|^2 = (\mathbf{E}^{w}_{out}) \cdot (\mathbf{E}^{w}_{out})^*, \tag{50}$$

with:
$$\mathbf{E}^{w}_{out} = \frac{E_0}{\sqrt{2}} e^{-i(\phi^{TE}_{ab}+\beta_{TE}L_0+\phi^{TM}_{fg}+\frac{\pi}{2})} \cdot [e^{-i(\beta_{TM}\frac{\Lambda}{2}+\pi)} + e^{-i\beta_{TE}\frac{\Lambda}{2}}] \cdot \frac{1}{\sqrt{2}}. \tag{51}$$

Hence:

$$\begin{aligned} I_{out} &= \left|\mathbf{E}^{w}_{out}\right|^2 = (\mathbf{E}^{w}_{out}) \cdot (\mathbf{E}^{w}_{out})^* \\ &= (\frac{E_0}{2})^2 [(e^{-i(\beta_{TM}\frac{\Lambda}{2}+\pi)} + e^{-i\beta_{TE}\frac{\Lambda}{2}}) \cdot (e^{+i(\beta_{TM}\frac{\Lambda}{2}+\pi)} + e^{+i\beta_{TE}\frac{\Lambda}{2}})] \\ &= \frac{E_0^2}{4}[1 + e^{-i(\beta_{TM}\frac{\Lambda}{2}+\pi-\beta_{TE}\frac{\Lambda}{2})} + e^{-i(\beta_{TE}\frac{\Lambda}{2}-\beta_{TM}\frac{\Lambda}{2}-\pi)} + 1] \\ &= \frac{E_0^2}{4}[2 + 2(\frac{e^{-i[(\beta_{TM}-\beta_{TE})\frac{\Lambda}{2}+\pi]} + e^{+i[(\beta_{TM}-\beta_{TE})\frac{\Lambda}{2}+\pi]}}{2})] \\ I_{out} &= \frac{E_0^2}{4}(2 + 2\cos[(\beta_{TM}-\beta_{TE})\frac{\Lambda}{2}+\pi]).\end{aligned} \tag{52}$$

For phase-matched wavelength $\lambda=\lambda_0$, $\Lambda = \frac{\lambda_0}{\Delta n}$.

Therefore:
$$(\beta_{TM}-\beta_{TE})\frac{\Lambda}{2} = \frac{2\pi}{\lambda}\Big|_{\lambda=\lambda_0} \cdot (n_e - n_o) \cdot \frac{1}{2}\frac{\lambda_0}{\Delta n} = \pi,$$

hence: $$I_{out} = \frac{E_0^2}{4}(2 + 2\cos(2\pi)) = \frac{E_0^2}{4}(2+2) = E_0^2 .$$

And if $\lambda \neq \lambda_0$, phase match condition is not satisfied and mode conversion does not occur, causing the total phase difference between the upper and lower arm to be π at the output point "g". Hence, $I_{out} \to 0$.

By similar procedure, when the incident light is TM polarized, we also get $I_{out} = E_0^2$ for phase matched wavelength $\lambda=\lambda_0$ and $I_{out} = 0$ otherwise. In summary, for any polarized light at the input, the filter will route the light to the output only if the wavelength satisfies the phase match condition. If the phase match condition is not satisfied, the second-order (asymmetric) mode is encountered in the output branch and will be cut off by the single-mode output waveguide [15].

Fig. 8 illustrates this behavior in a symmetric Mach-Zehnder interferometer structure.

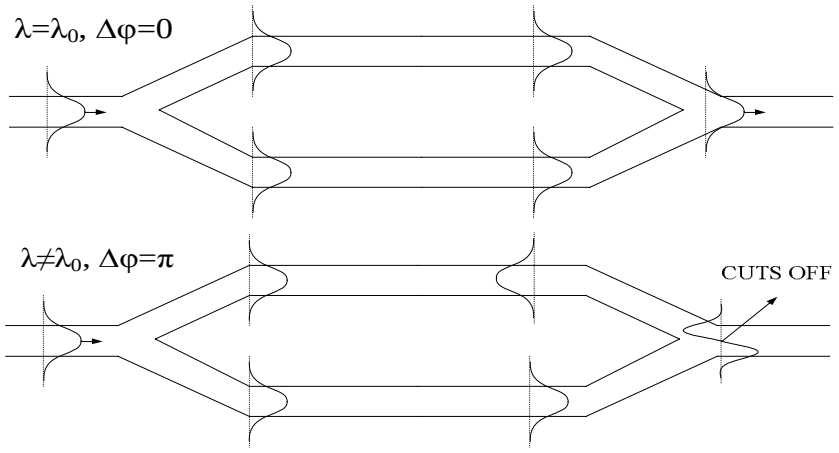

Fig. 8. Operation of the symmetric interferometric modulators with zero phase difference between the arms and π phase difference.

CHAPTER IV

DEVICE FABRICATION

Several samples were processed in the course of device fabrication. The parameters that were used for control include titanium (Ti) layer thickness, diffusion temperature and diffusion time. A step-by-step outline of the process is listed in Appendix 1. The process sequence for fabrication is described in this chapter.

A. Ti:$LiNbO_3$ Channel Waveguides and Mach-Zehnder Interferometers

The fabrication of channel waveguides and Mach-Zehnder interferometers begins with dicing substrates to appropriate sizes. 1mm thick, 3-inch diameter, x-cut $LiNbO_3$ crystal wafers supplied by Crystal Technology Inc. (Palo Alto, CA) were diced into small pieces (Appendix 2) for making waveguides with propagation in y-direction. The diced samples were cleaned with liquid solvent (Appendix 3) first, and then a thin film of Ti was deposited over the entire crystal surfaces using DC Sputtering process (Appendix 4). After deposition, channel waveguides and Mach-Zehnder interferometers patterns were delineated in photoresist by positive photolithography process (Appendix 5). The photoresist patterns were visually inspected under a microscope to ensure the quality of the pattern.

Once satisfactory patterns were developed, the samples were further cleaned in O_2

plasma (Appendix 6) for 3 minutes, and vacuum hard bake at 135°C for 5 minutes to harden the photoresist. The exposed Ti film was etched using reactive ion etching (RIE, Appendix 7). Because the gases (CHF_3 75 sccm, argon 2 sccm, helium 7.5 sccm) used in plasma etching would slightly etch the substrate materials if over etched, it was important to etch the Ti film to such extent that there was still a very thin layer of Ti left after RIE to protect the surface of substrates [13]. The residual Ti film was etched using diluted hydrofluoric (HF) acid. Since Ti is easily oxidized in air, a thin layer of titanium oxide is always present on the Ti surface. This oxide layer reacts in the HF very slowly. Once the oxide is etched away, the corrosion of the pure Ti goes rapidly and this makes the wet etching process hard to control. Over etching may lead to Ti undercutting which results in narrower waveguides with rough edges. A rough waveguide edge will induce scattering losses. Appropriate acid solution and wet etching time is required to achieve a good etching result. For a 1050Å~1100 Å Ti layer, 1:25 HF:DI water and 10~13 seconds etching time was found to work good.

After etching, the remaining photoresist was removed in heated (90°C) photoresist stripper (Clariant AZ 300T) leaving the desired strip of Ti. Then the samples were cleaned with solvent solution following the same process mentioned earlier (Appendix 3). The structure of an asymmetric Mach-Zehnder interferometer is shown in Fig. 9 and further detailed description can be found in Appendix12 & 13.

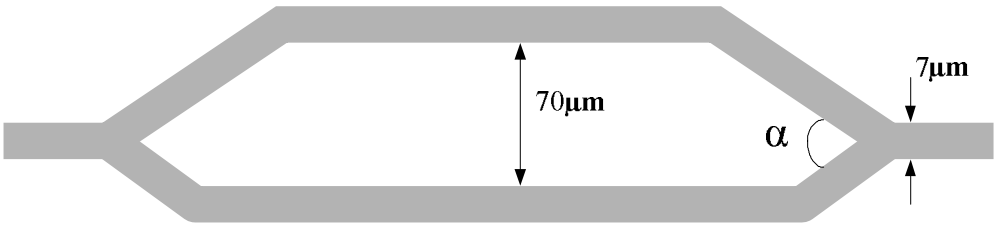

Fig. 9. Asymmetric Mach-Zehnder Interferometer layout with splitting angle of α.

The width of the Ti waveguide and the Y-branch was checked using a microscope, and the thickness of Ti strip was measured using Dektak^3 Surface Profile Measuring System. The pattern near the Y-branch is critical, because the angle α in the splitter is small (~1°). To make a satisfactory pattern, parameters in positive photolithography (UV light exposure time, developing time, etc) and in dry and wet etching have been optimized.

The samples were then placed in a diffusion furnace for diffusion at certain temperature from 1025°C to 1050°C for typical times of 10~13 hours in wet air ambient (Appendix 8). The wet air ambient treatment was used to reduce Li_2O out-diffusion [16, 17], which can cause unwanted planar guiding for the extraordinary polarization [10] and lead to significant increase in the propagation loss (in our case, TE mode).

The diffusion temperature T and diffusion time t are two key control parameters to make a good waveguide, which guides both TE and TM light well. The diffusion temperature is more important than the diffusion time t as shown in the following equation [10]:

$$d = 2(Dt)^{1/2}, \tag{53}$$

where d is the diffusion depth and $D = D_0 e^{(-T_0/T)}$. D_0 and T_0 depend upon the lithium niobate composition. For commonly used $LiNbO_3$ (48.6 mole % of Li_2O), representative values are [18] $T_0 \approx 2.5\times10^4 K$ and $D_0 \approx 2.5\times10^{-4} \frac{cm^2}{s}$.

At last, the samples were edge polished to an optical finish (Appendix 9) along the two end faces perpendicular to the waveguides. A good optical finish and a 90° edge are required at both the input and output optical facets to ensure good fiber-to-waveguide coupling [19]. The more advanced industry practice is to polish the substrate end surface at an angle to the waveguides in order to eliminate reflection.

B. Electro-Optically Tunable Wavelength Filter

The electro-optically tunable wavelength filters were produced on samples with size 13mm (z-axis) by 36mm (y-axis). A schematic diagram of the sample structure is illustrated in Fig. 6 in Chapter III. A complete device consists of three layers: Ti in-diffused waveguides, metal electrodes and SiO_2 grating pads:

First, Ti in-diffused Mach-Zehnder interferometers and straight channel waveguides were produced on $LiNbO_3$ substrate following the process as described in Section A.

Second, electrodes pattern with width of 13μm and gap of 17μm for both upper and lower arms were delineated in photoresist using image reversal photolithography process (Appendix 10). Then metal layers (Cr/Au/Ti) of thickness 800Å/600Å/800Å were deposited on the samples surface using E-Beam evaporation (Appendix 11). The Cr layer

was used to improve the adhesion with the $LiNbO_3$ substrate and Ti was used to prevent Au from diffusion into the SiO_2 in later process. The electrodes patterns were formed by liftoff in acetone.

Third, once the interferometer waveguides and electrodes were produced, a layer of SiO_2 with thickness of 1.5μm [20] was deposited by E-Beam evaporation in O_2 atmosphere at 360°C temperature. After deposition, the samples were allowed to slowly cool down in O_2 before removing from the chamber. The injected O_2 during hot deposition and cooling down was intent to prevent out-diffusion of oxygen from the substrate. Positive photolithography was used to delineate the grating patterns (see Appendix 14 for detailed dimensions) afterwards. Then the samples were vacuum hard baked at 135°C for 30 minutes and etched in the RIE system for 19 minutes. The remaining unwanted SiO_2 film was removed by buffered oxide etch (BOE) solution for ~1.5minute.

CHAPTER V

OPTICAL TESTING AND RESULT ANALYSIS

In this chapter, the optical testing results of straight channel waveguides, Y-branch optical power splitter and combiner, electro-optical modulation of asymmetric Mach-Zehnder interferometers, and polarization mode converter are given. The performance of two-port wavelength tunable filter is also presented.

A. Channel Waveguide

Good quality channel waveguides are the basis for the electro-optically tunable filter. A good quality waveguide means low insertion loss for both TE and TM polarized light, where insertion loss means the total amount of optical intensity lost through a device and is defined as

$$\text{Insertion loss (dB)} = \text{-}10 \cdot \log \frac{P_{out}}{P_{in}}. \tag{54}$$

Waveguide insertion loss is a combination of propagation loss, Fresnel loss and mode mismatch loss. Fresnel loss, or in other words Fresnel reflection loss, is due to the reflection at the two end interfaces of the substrate. It can be express as the following

$$\text{Fresnel loss(dB)} = -2 \cdot 10 \cdot \log \left[1 - \left(\frac{n-1}{n+1} \right)^2 \right] \tag{55}$$

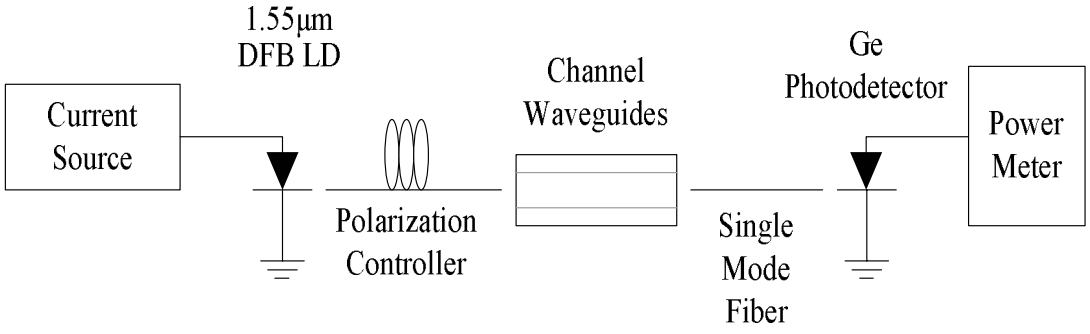

Fig. 10. Testing setup for insertion loss measurement.

The schematic diagram of the optical testing setup for the insertion loss measurement is shown in Fig. 10. A pigtailed 1.55μm DFB laser diode driven by current source (ILX Lightwave, Model LDX-3412) at 32mA was used as the optical power source. The laser diode was spliced to a single mode fiber (Corning SMF-28^{TM}) and then passed through a fiber polarization controller (Thorlabs Inc., Model FDC 10), which was used to control the polarization state of the light launched into the device. The emerging light at the output of the device was butt coupled to another single mode fiber. The output light from the fiber was detected by a Ge photodetector (Newport, Model 818-IR), which is connected to a power meter (Newport, Model 1825-c).

Several samples were fabricated with different thickness, waveguide width and diffusion conditions. A summary of the insertion loss measurement results for sample K11 (sample length=13mm, Ti thickness=1059Å, 11 hours diffusion at 1025°C) is given in Fig. 11. It is obvious from the graph that waveguides with width 7μm and 8μm guide well both the TE mode and TM polarization.

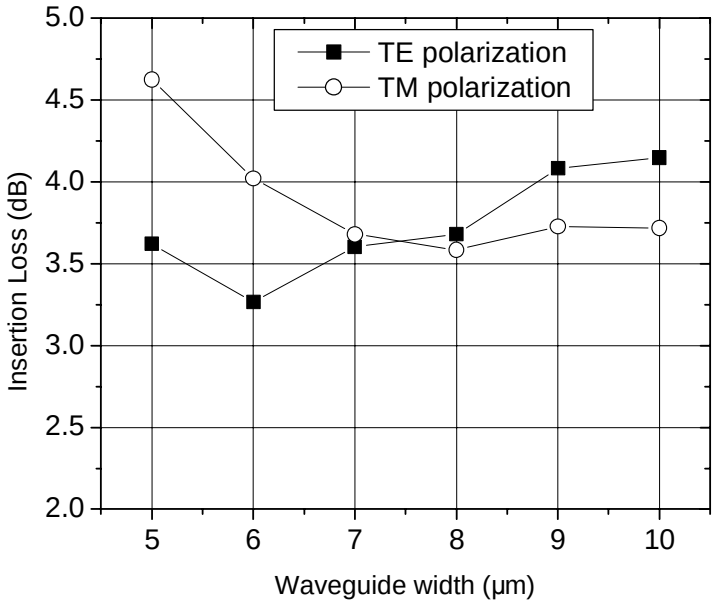

Fig. 11. Insertion loss variation with waveguide width for sample K11,
Ti thickness=1059Å, diffused at 1025°C for 11 hours.

A summary of the insertion loss variation with different diffusion time for 7μm and 8μm wide waveguides on sample K11 is presented in Table 2. After 10 hours of diffusion at 1025ºC, both 7μm and 8μm waveguides were weakly guiding and loss for both the TE and TM polarization were large. After additional diffusion in intervals of one hour, the insertion loss tended to drop for the 7μm waveguide from 10 hours to 10+1+1 hours, while for 8μm waveguide, insertion loss decreased from 10 hours to 10+1 hours and started to increase after 10+1+1 hours.

Table 2. Insertion loss on sample K11 (7μm- and 8μm-wide waveguide).

Waveguide width \ Diffusion time		10 hours	10+1 hours	10+1+1 hours
7 μm	TE	4.3470	3.6032	3.4242
	TM	4.1697	3.6798	3.4887
8 μm	TE	4.6661	3.6798	3.7173
	TM	4.5319	3.5843	3.5920

Another important feature for characterizing channel waveguides is the near field intensity mode profile. The testing setup is illustrated in Fig. 12. At the input side, it is the same as the one for insertion loss measurement. At the output end, a vibrating mirror and a 100 μm wide slit was used to translate the output beam across a Ge photodetector. The mode profile image was displayed on an oscilloscope and by Labview program on a computer. The data can be stored via a NI-DAQ (National Instruments-Data Acquisition)

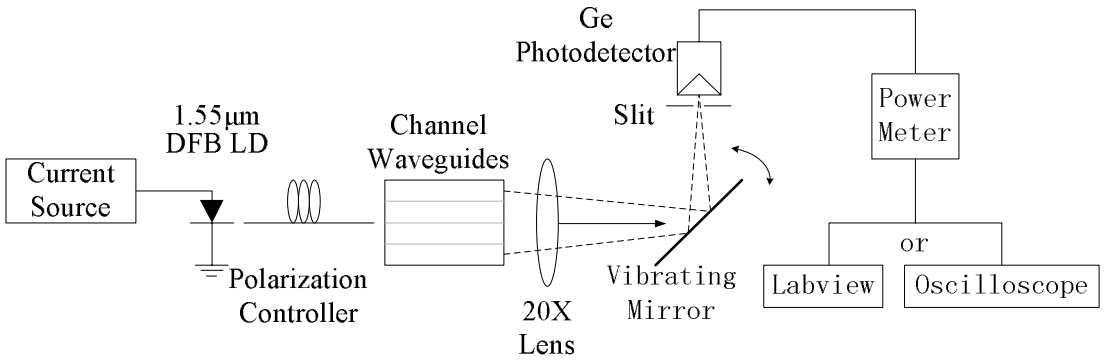

Fig. 12. Testing setup for mode profile measurement.

board. For horizontal scans the slit was oriented vertically. For vertical scans the slit was oriented horizontally.

To evaluate the mode confinement of channel waveguides, Full Width at Half Maximum (FWHM) was used. The measured near field mode profile on sample K11 (7μm) is shown in Fig. 13 for both TE and TM mode. It is evident that single mode is supported in the channel waveguide, since there is only one peak in display. The horizontal scan mode profiles are symmetric and show a Gaussian shape distribution. The vertical scan mode profiles are asymmetric, which correspond to the asymmetric waveguide structure in the vertical direction (air, Ti and $LiNbO_3$ substrate, see Fig. 5).

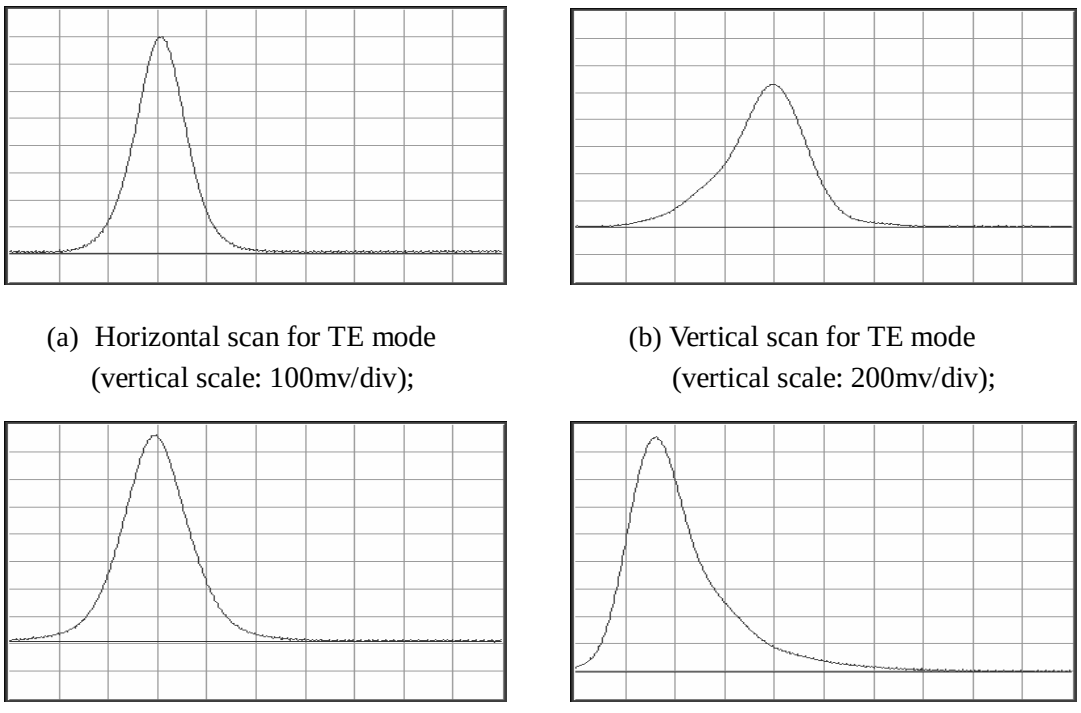

(a) Horizontal scan for TE mode (vertical scale: 100mv/div);

(b) Vertical scan for TE mode (vertical scale: 200mv/div);

(c) Horizontal scan for TM mode (vertical scale: 100mv/div);

(d) Vertical scan for TM mode (vertical scale: 100mv/div).

Fig. 13. Mode profile for 7μm waveguide on sample K11 (horizontal scale: 4.56μm/div).

To measure FWHM, a directional coupler (sample G282, set No.6) with two-output arms separation of 68μm was used to as a standard scale. And the measured FWHM of the 7μm wide waveguide (sample K11) is given in Table 3.

Table 3. Measured FWHM for 7μm wide waveguide on sample K11 with 1059Å Ti thickness and 12 hours diffusion at 1025ºC temperature.

	TE mode	TM mode
Horizontal FWHM (μm)	5.48	6.46
Vertical FWHM (μm)	6.34	5.61

B. Optical Power Splitter/Combiner

The optical power splitter and combiner (Y-branch) are key elements for the electro-optically tunable filter. Several samples were fabricated to test the performance of the splitter/combiner. Optical testing was carried out in two ways. First, incident light was launched at the one-port end and output power from the two ports at the other end were measured (Fig. 14(a)). Second, the sample position was reversed and incident light

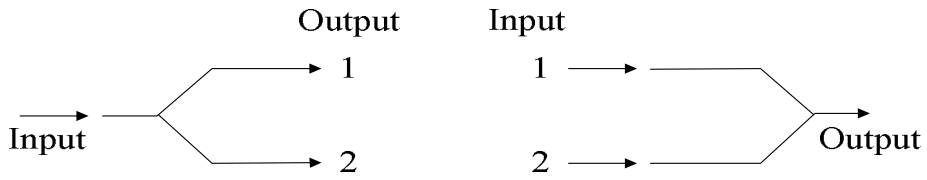

(a) Optical power splitter (b) Optical power combiner

Fig. 14. Two ways for characterizing Y-branch power splitter/combiner.

with same input power was launched into each of 2 ports individually and the emerging light power from the single output port for each case was measured (Fig. 14(b)).

Table 4. Output power of Y-branch testing on sample P211 with Ti thickness of 1050Å, diffused @ 1025°C for 9+1+1 hours, P_{in}=1.71mw.

Device	I1		I2		I3		I4		I5		I6	
	a	b	a	b	a	b	a	b	a	b	a	b
9 hrs	303	280	266	275	311	307	305	300	330	300	320	300
9+1hrs	320	330	290	289	313	325	316	355	337	330	328	325
9+1+1hrs	320	327	276	286	333	338	326	312	330	324	312	290

(a) TE input, splitter

Device	I1		I2		I3		I4		I5		I6	
	a	b	a	b	a	b	a	b	a	b	a	b
9 hrs	280	280	255	267	306	307	290	280	305	290	300	270
9+1hrs	325	335	285	290	310	330	310	340	340	335	336	330
9+1+1hrs	300	316	270	293	306	313	320	319	318	288	319	303

(a) TE input, combiner

Device	I1		I2		I3		I4		I5		I6	
	a	b	a	b	a	b	a	b	a	b	a	b
9 Hrs	241	230	230	226	226	225	220	210	210	195	210	200
9+1	279	270	255	270	271	273	280	270	270	265	270	251
9+1+1	301	286	285	270	277	280	303	297	300	282	292	272

(c) TM input, splitter

Device	I1		I2		I3		I4		I5		I6	
	a	b	a	b	a	b	a	b	a	b	a	b
9 Hrs	245	235	232	225	225	220	210	203	212	202	200	185
9+1	280	275	255	272	265	270	277	263	276	266	263	243
9+1+1	290	272	288	272	283	285	310	300	300	276	278	255

(d) TM input, combiner

Sample P211 was fabricated to characterize the splitter/combiner performance and the testing results are summarized in Table 4.

C. Electro-Optic Modulation

To ensure the electrooptic tuning ability of final filter components, electrooptic intensity modulation of the asymmetric Mach-Zehnder interferometers was investigated by impressing an external electrical field across one arm of the interferometer. The electrical field was impressed by applying a DC voltage across a pair of electrodes centered on the waveguide arm. The sample structure for electro-optic modulation testing is illustrated in Fig. 15.

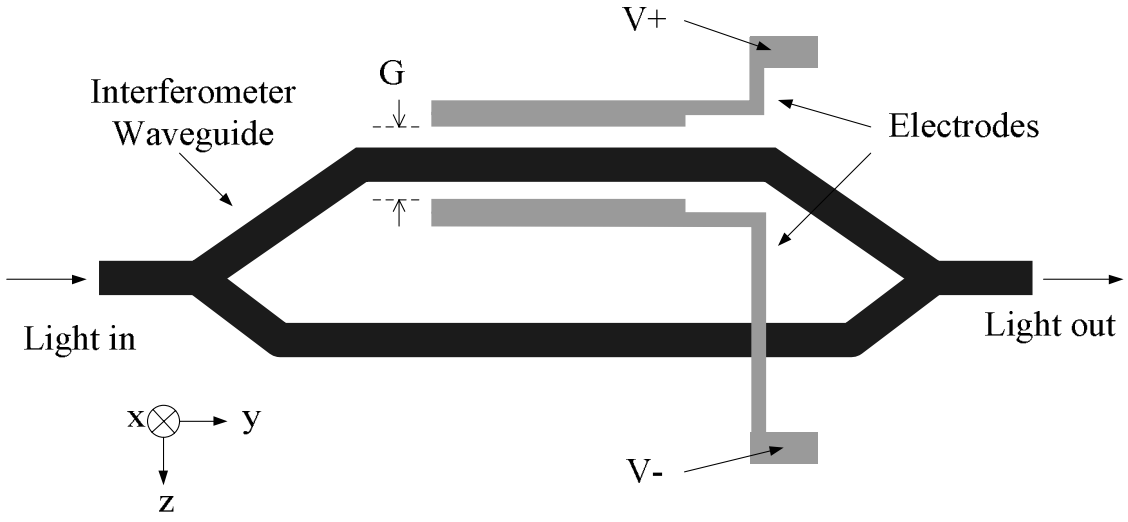

Fig. 15. Device structure for electro-optic effect testing.

For an applied field along the z axis, and from equation (21), the electro-optically induced index changes are

For TE: $$\Delta n_e = -\frac{n_e^3}{2} r_{33} \frac{V_T}{G} \Gamma_{TE}$$

for TM: $$\Delta n_o = -\frac{n_o^3}{2} r_{13} \frac{V_T}{G} \Gamma_{TM} \quad (56)$$

where V_T is the applied voltage, G is the interelectrode gap, Γ_{TE} and Γ_{TM} are overlap factors between the applied electrical field and the optical field. Assuming the interaction length is L, the total phase shift can be expressed as

$$\Delta\phi = \Delta\beta L = -\pi n^3 r \Gamma \frac{V_T}{G} \frac{L}{\lambda} \quad (57)$$

where n is either n_e or n_o, and r represents the relevant electrooptic coefficient r_{33} or r_{13}.

For $LiNbO_3$ n_e=2.20, n_o=2.29, $r_{33} = 30.8\times10^{-12}\ m/V$, $r_{13} = 8.6\times10^{-12}\ m/V$.

Thus, the required voltage for a π-radian phase shift can be expressed as

$$V_\pi = \frac{\lambda G}{n^3 r L \Gamma}. \quad (58)$$

Table 5. Performance of electro-optic modulation on sample P123
(Ti thickness=1095 Å, diffused @ 1025°C for 10 hours).

Input polarization	TE mode	TM mode
Interaction length (mm)	11	11
V_π (V)	14.9	44
Maximum output (μw)	300	105
Minimum output (μw)	1.3	1.1
Modulation depth	99.6%	98.9%

Sample P123 was fabricated to investigate the electro-optic intensity modulation. A thin metal layer (Cr/Al) was deposited on the sample surface after Ti in-diffused interferometer waveguides were produced, and an electrode pattern with interaction length of 11mm and gap G=17μm was delineated by lift-off process (see Chap. IV for detail). The input optical power was 1.71mW and the output power was measured while voltage was applied across the electrodes. Table 5 summarizes the modulation results on sample P123.

D. TE↔TM Mode Converter

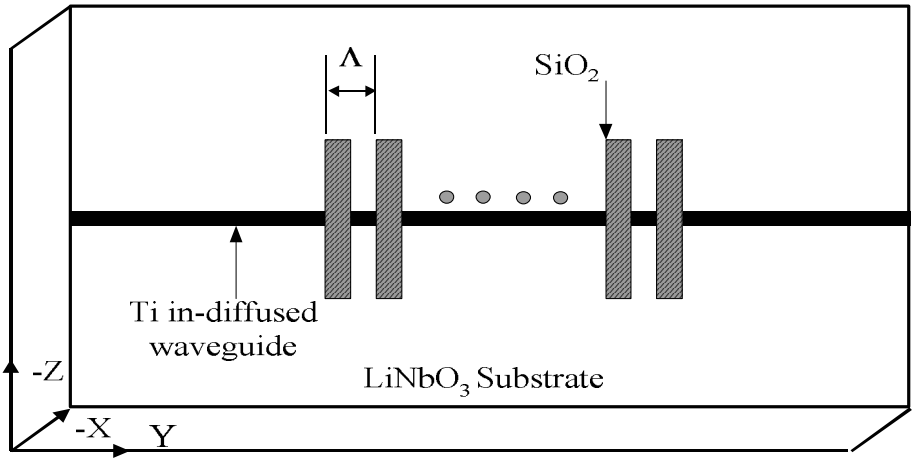

Fig. 16. Mode converter device structure.

To evaluate TE↔TM mode converters (see Fig. 16), optical testing was carried out using light from a broadband light source. The setup is shown schematically in Fig. 17.

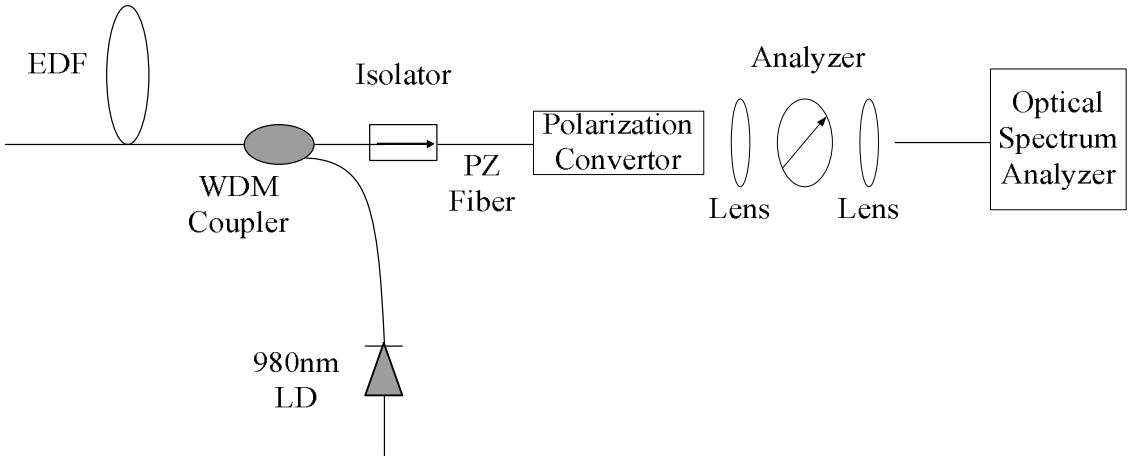

Fig. 17. Testing setup for mode converter.

A 10m long erbium-doped fiber (EDF) was pumped by a 980nm laser diode (Lasertron, MA, Model QLM9S473-217) through a WDM coupler and Amplified Spontaneous Emission (ASE) light from the Erbium-Doped Fiber Amplifier (EDFA) was used as the broadband light source. An optical isolator was included at the output of the coupler to prevent external cavity self-oscillation. The light was then guided though a polarizing fiber (PZ fiber), whose end can be rotated to select either TE or TM polarization input to the device. The output light from the device was collimated by an objective lens (20×) and passed through a polarization analyzer, which can be set to either TE or TM mode by rotation. Afterwards, the light beam was focused by another objective lens (20×) and was coupled into a single mode fiber. The output light spectrum from the fiber was observed on an Optical Spectrum Analyzer (OSA, Anristru, Model MS9710C). Fig. 18 shows the ASE output spectrum driven at 60mA.

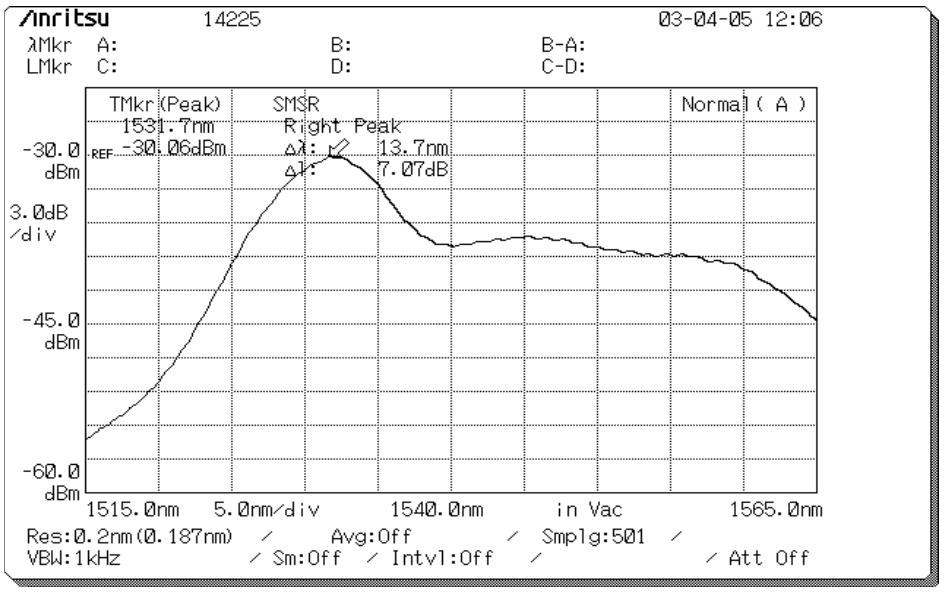

Fig. 18. Spectral density as a function of wavelength for the ASE output driven at pump current of 60mA.

To test TE↔TM conversion, the input PZ fiber was set to either TE or TM polarization and the output power for TE and TM mode was measured by rotating the analyzer to choose either TE or TM. TE→TM or TM→TE mode conversion efficiency can be determined by

$$\text{TE input}: \ \eta = \frac{P_{TM}}{P_{TM}+P_{TE}}$$
$$\text{TM input}: \ \eta = \frac{P_{TE}}{P_{TE}+P_{TM}} \qquad (59)$$

where P_{TE} and P_{TM} are the output power of TE and TM mode, respectively.

The output spectrum of a mode converter on sample P215 for TE input is shown in Fig. (19). Sample P215 with 7μm wide channel waveguide was produced by diffusing 1080Å thick Ti film at 1025°C for 12hours. 500 SiO_2 strain grating pads with spatial

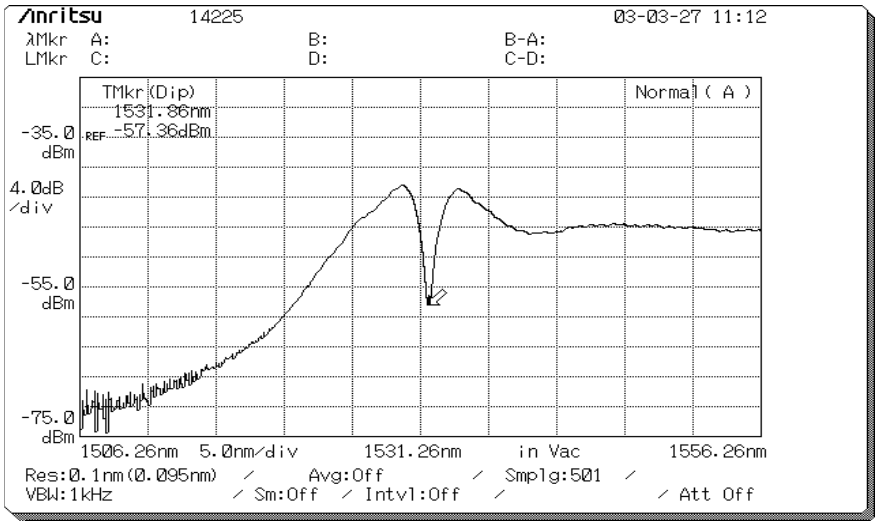

(a) unconverted (TE) mode output spectrum

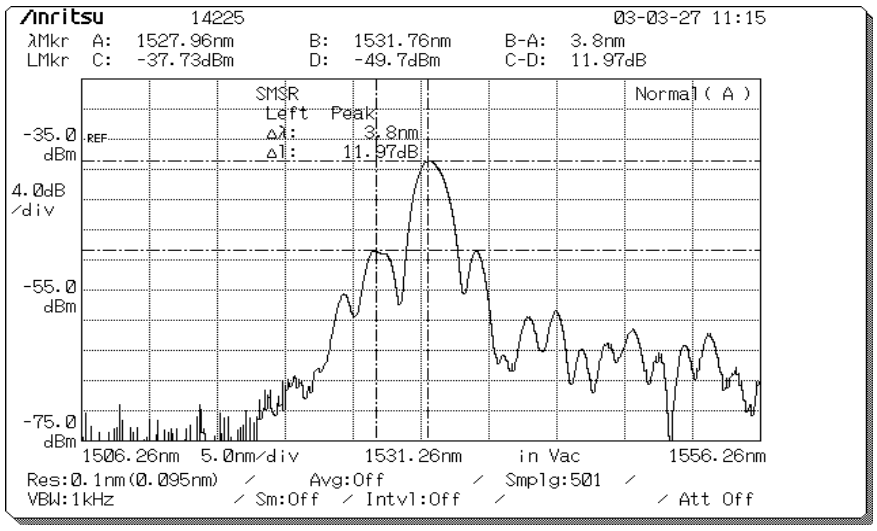

(b) converted (TM) mode output spectrum

Fig. 19. Output spectrum of mode converter (sample P215) with TE polarization input.

period Λ=21μm was delineated on the surface. The SiO_2 film was deposited at 360°C to a thickness of 1.25μm and patterned after cool off to room temperature. Fig. (19a) shows the unconverted (TE) output spectrum and Fig. (19b) shows the converted (TM) output. As shown, the mode conversion is wavelength dependent and the maximum

conversion is at 1531.86nm, indicating a birefringence $|\Delta n|$ of 0.0729 for Λ=21μm from equation (36). The 3-dB bandwidth is 2.24nm as indicated in Fig. 20(a) and is in close agreement with the value of 2.44nm calculated from the relation [21]

$$\Delta\lambda = 0.8\frac{\lambda_0}{N} \tag{60}$$

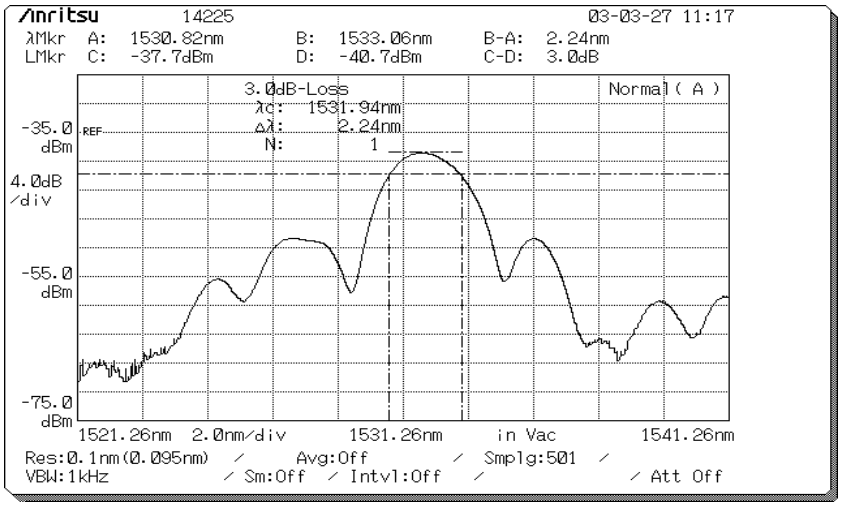

(a) TE→TM

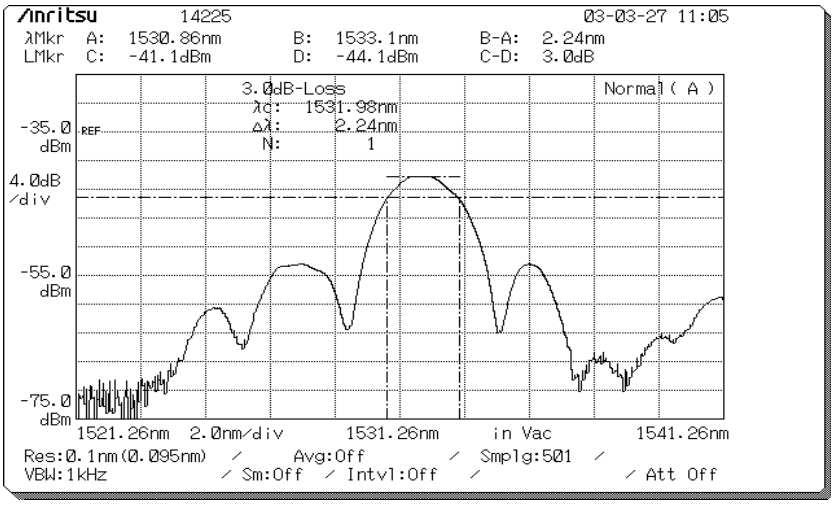

(b) TM→TE

Fig. 20. 3-dB bandwidth of the mode converter.

where N is number of grating pads (N=500 in our case). Optical testing was carried out for TM→TE conversion as well, and is shown in Fig. 20(b).

The polarization conversion efficiency was evaluated independently by coupling TE or TM polarized light at the input port and was calculated using equation (59). The spectral response of TE↔TM conversion efficiency is shown in Fig. 21. The maximum conversion efficiencies are 98.9% for TE→TM and 98.0% for TM→TE, both observed at 1531.86nm.

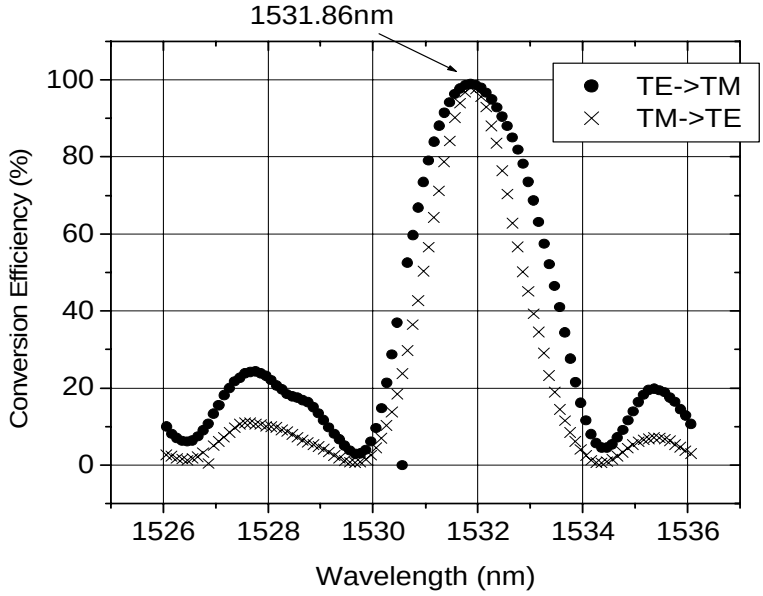

Fig. 21. The mode conversion efficiency as a function of wavelength for TE and TM input.

E. Electro-Optically Tunable Filter

Based on the obtained results for electro-optic modulation and mode conversion, one complete sample (P123) having filters of the configuration illustrated in Fig. 6 was

produced following the procedure described in Chap. IV. The waveguides were fabricated on x-cut, y-propagating $LiNbO_3$ by in-diffusion of 7μm wide 1095Å thick Ti stripes for 10 hours at 1025°C in wet air ambient. The end facets of the sample were then polished. The final length of the sample after polish was 35mm. Electrodes 13μm wide centered about the arms of the interferometer with a gap of 17μm were next formed by liftoff using Cr/Au/Ti (800Å/600Å/800Å) metal films. The strain induced index grating was produced by e-beam deposition of 1.5μm thick SiO_2 film at 360°C and pattering after cool down to room temperature. A total of 500 strain inducing SiO_2 pads with a spatial period Λ=21μm were delineated on each arm of the interferometer, with an offset of half a spatial period, $\Lambda/2$, for the position of the first pad on one arm relative to the other arm. The filter characteristics were evaluated using a polarized broadband source for input and an OSA at the output. Thermal and electrical tuning were examined. A DC voltage supply was used for electro-optic tuning.

E-1. Bandwidth and side-lobe characteristics

The output spectrum of device I#4 on sample P123 without an applied voltage at room temperature is shown in Fig. 22. The center wavelength is at 1531.0nm for TE polarization input, 1531.2nm for TM polarization input and 1531.5nm for input light polarized at 45° between TE and TM. The –3dB bandwidth is 2.4nm which is close to the expected value of 2.44nm calculated from $\Delta\lambda = 0.8 \cdot \lambda_0 / N$. The measured response

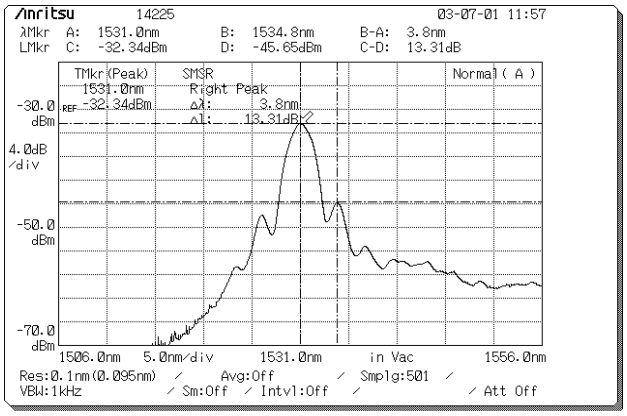

(a) TE input, λ_c=1531.0nm, FWHM=2.36nm

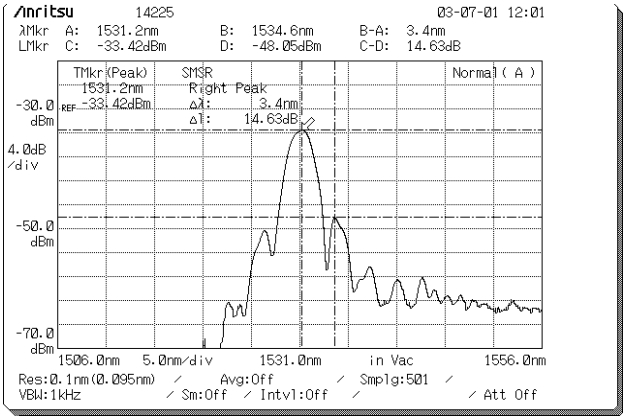

(b) TM input, λ_c=1531.2nm, FWHM=2.4nm

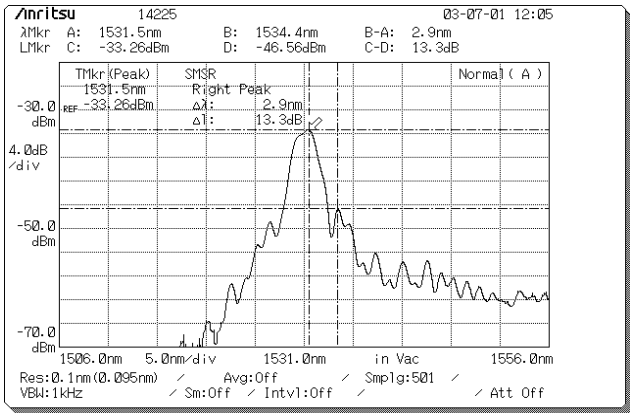

(c) 45° input, λ_c=1531.5nm, FWHM=2.4nm

Fig. 22. The filter output spectrum for device I#4 on sample P123 without applied voltage at room temperature, driven at pump current of 60mA.

shows the side lobes are 13dB from to the main peak.

Fig. 23 shows the output spectrum in relative power for device I#4 (sample P123). It is obtained by normalizing the filter output power $P_F(\lambda)$ relative to the output power of the broadband source of the erbium doped fiber (EDF) from a straight channel waveguide $P_{EDF}(\lambda)$, both acquired through the OSA for the same pump drive current of the EDF. The resultant values are then divided by the ratio of the filter maximum output power at the center wavelength $P_{Fmax}(\lambda_c)$ to the erbium fiber output power from the straight channel waveguide at same λ_c, and expressing the results in dB, i.e.

$$10\times\log_{10}\left[\frac{\left(P_F(\lambda)/P_{EDF}(\lambda)\right)}{\left(P_{Fmax}(\lambda_c)/P_{EDF}(\lambda_c)\right)}\right].$$

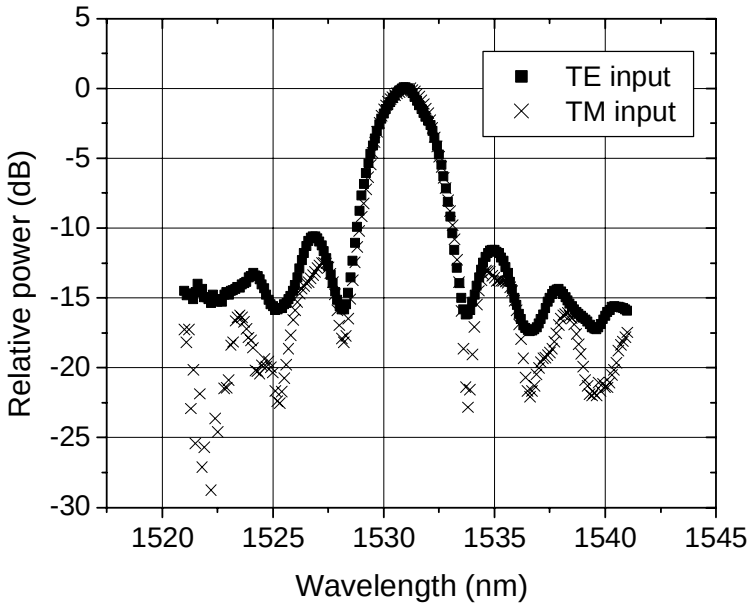

Fig. 23. The filter output spectrum for device I#4 on sample P123
at relative power compared to EDFA output spectrum.

E-2. Thermal tuning

Thermal tuning of the filter is accomplished by changing the substrate temperature, which results in the change of birefringence and the shift of phase-match wavelength. Fig. 24 shows the output spectrum of device I#5 on sample P110 (Ti thickness=1102Å, diffuse @ 1025°C for 12 hours) at room temperature and at 11.5°C, for TE input polarization. The center wavelength is 1532.8 nm at 23°C and shifts to 1541.6nm at 11.5°C, indicating a thermal tuning rate of –0.765nm/°C.

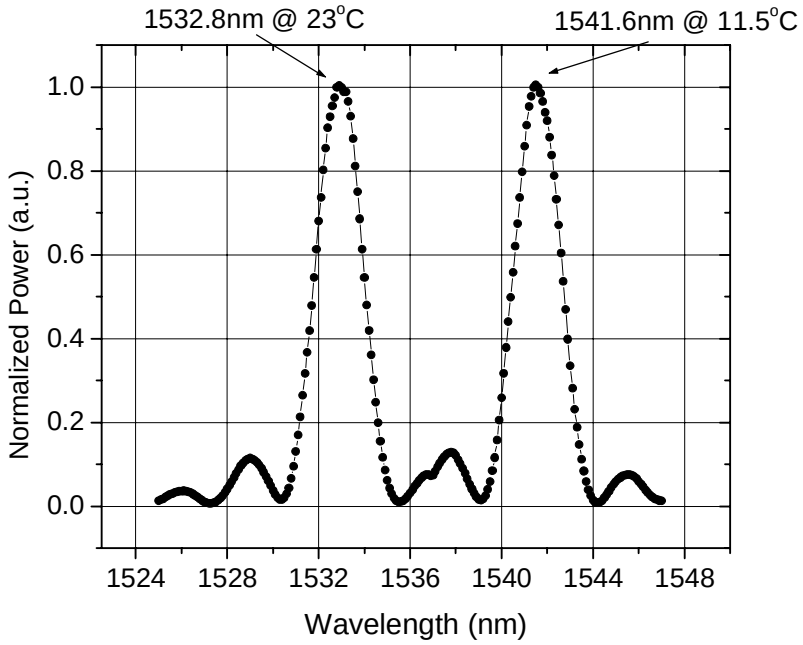

Fig. 24. Normalized thermal tuning characteristics of device I#5 on sample P110 at 23°C and 11.5°C, for TE input polarization.

E-3. Electrical tuning

Electrical tuning was carried out by applying DC voltage across the electrodes with

17μm gap. The voltage tuning rate for the wavelength of maximum filter transmission is given by [22, 23]

$$\frac{d\lambda}{dV_T} = \frac{1}{2}(\Gamma_{TE} n_e^3 r_{33} - \Gamma_{TM} n_o^3 r_{13}) \frac{\Lambda}{g}, \tag{61}$$

where V_T is the applied tuning voltage, Λ is the spatial period of the grating, g is the gap between the electrodes, Γ_{TE} and Γ_{TM} are overlap factors between the applied electrical field and the optical field for TE mode and TM mode, respectively.

Device I#1 on sample P123 was tested for phase-match wavelength as a function of applied tuning voltage V_T. The spectral response of the filter at 17°C is shown in Fig. 25, and indicates that the center wavelength shifts by 11.5nm by varying V_T from –80V to +60V.

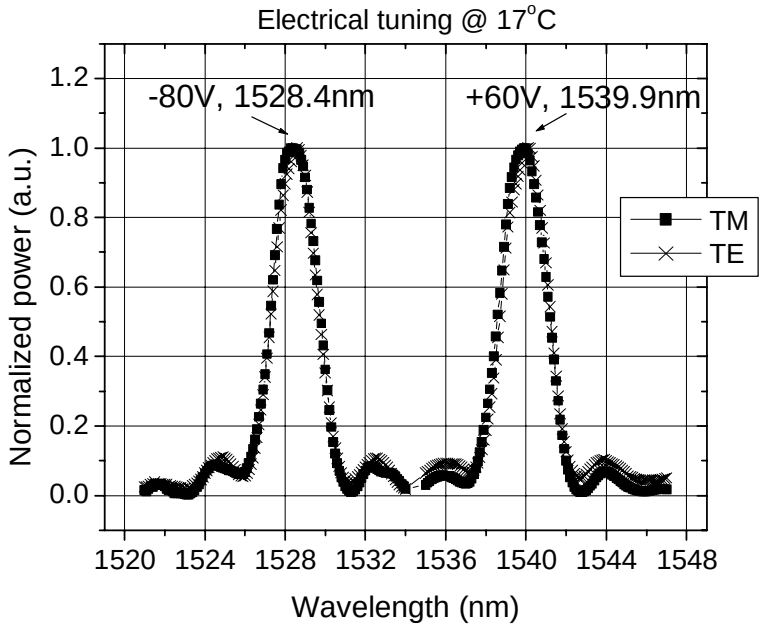

Fig. 25. Normalized electrical tuning characteristics of device I#1 on sample P123 at 17°C.

Fig. 26 shows the peak wavelength shift of the filter (I#1, sample P123) at 17°C for both TE and TM input polarization with applied voltage, and indicates a linear tuning rate of 0.08nm/V. A maximum tuning range of 12.8nm is achieved by changing the tuning voltage from -80V to +80V. As shown in Fig. 26, the peak wavelength shifts are off the fit straight line at high applied voltage. This is due to the fact that electrode patterns are not well centered on the waveguide which causes a nonuniform electrical field along the tuning region. The tuning range is limited by the breakdown field of $LiNbO_3$ (nearly 10V/μm) [11]. Assuming $\Gamma_{TE}=\Gamma_{TM}$, a value of 28.8% for the overlap factor is calculated from the equation (61).

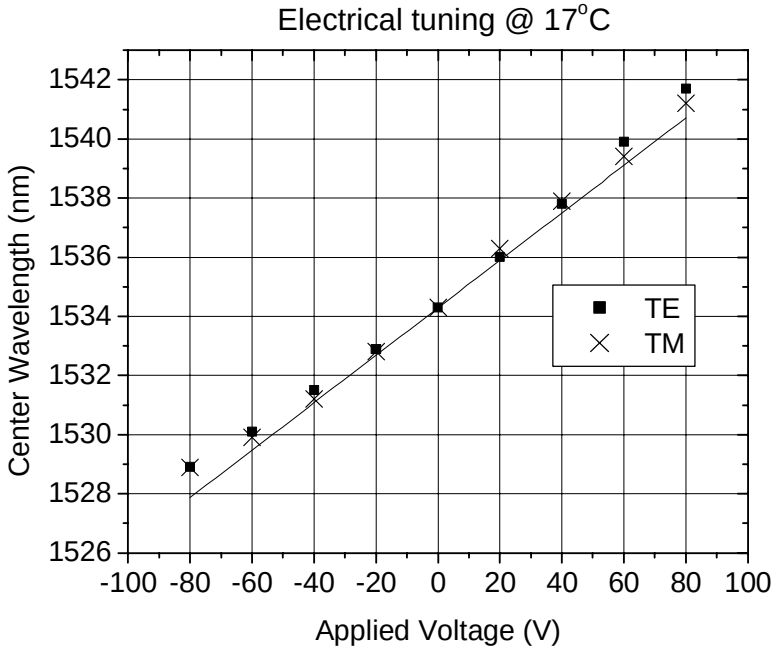

Fig. 26. Electrical tuning performance for device I#1 on sample P123 at 17°C.

Fig. 27 shows the peak wavelength shift of the filter (I#1, sample P123) at room temperature for both TE and TM input polarization with applied voltage, and indicates a tuning rate of 0.08nm/V which is the same as that obtained at 17°C.

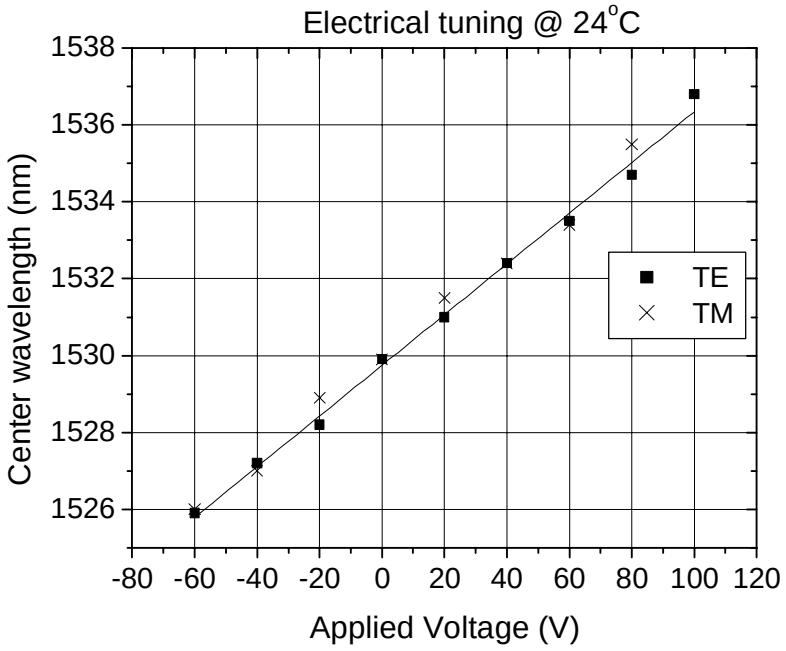

Fig. 27. Electrical tuning performance for device I#1 on sample P123 at 24°C.

F. Suggestion for Future Work

An important expansion of this research is a tunable four-port polarization independent optical add-drop filter. The design is demonstrated in Fig. 28. It consists of one directional coupler near the input side, another one near the output side, one pair of electrodes and two static strain-induced phase-matched polarization converters. It differs from the conventional filters design in the following respects [3]: (1) polarization beam

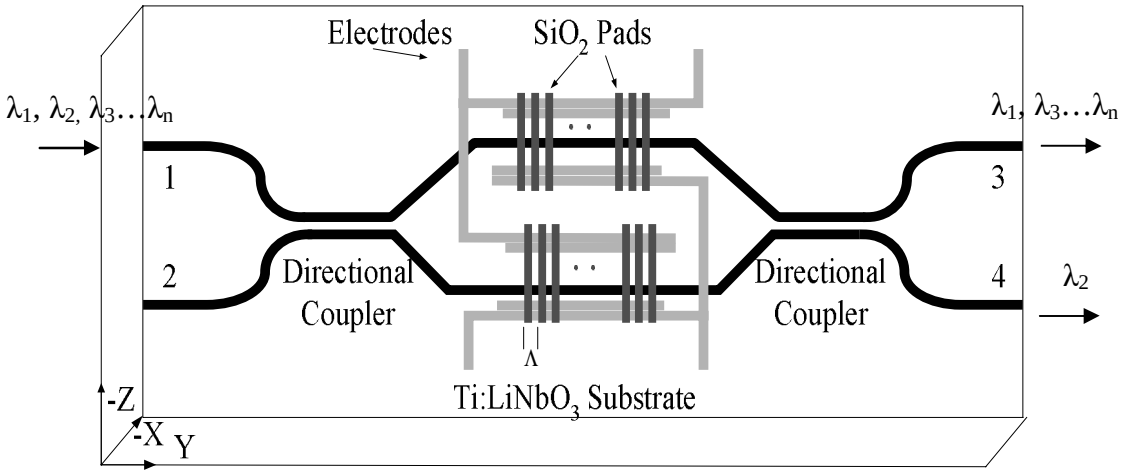

Fig. 28. New EOTF design.

splitters (PBS's) are not required; (2) the optical path difference between the two waveguide arms of the interferometer is half-wavelength; (3) the relative positions of the polarization coupling regions in the two waveguides arms are displaced in the propagation direction by half of the spatial period of the perturbation responsible for polarization coupling. The 2nd and 3rd features have been demonstrated in this research.

In this structure, an incident wavelength-multiplexed signal (λ_1, λ_2, λ_3,…λn) into port 1 would drop only a phase-matched wavelength (say λ_2) to output 4, and all other wavelengths would emerge from output 3. The drop wavelength can be selected by means of an applied tuning voltage through the surface electrodes.

CHAPTER VI

CONCLUSION

Electro-optic tunable filters (EOTFs) are enabling technology for WDM systems. For that purpose, two-port electro-optically wavelength tunable filters based on asymmetric Mach-Zehnder structure in $LiNbO_3$ substrate using Ti-indiffusion technology has been developed for 1.55μm application. To produce the filter, fabrication parameters for channel waveguides, interferometer waveguides and polarization converters were optimized.

Straight channel waveguides 7μm in width were produced by diffusing 1050-1100Å thick Ti into $LiNbO_3$ substrate at 1025°C. Single mode guiding has been realized for both TE and TM polarization. Insertion loss of 3.42dB for TE polarization and 3.48dB for TM polarization were achieved on 13mm long samples.

Mach-Zehnder interferometer performance was characterized by testing the Y-branch on samples of half length compared to complete devices. Devices were produced with Ti film thickness varying between 1050Å~1100Å. The relation between insertion loss and diffusion time was investigated. Best results were obtained from samples that were produced by diffusion at 1025°C for 11 hours of 1050Å thick Ti film, and by diffusion at 1025°C for 12 hours of 1090Å thick Ti film.

Metal electrodes were added on sample P123 with unbalanced Mach-Zehnder

interferometers to evaluate electro-optic modulation. The optical test was carried out by applying DC voltage across a pair of electrodes centered on one waveguide arm and by measuring the output optical power. Modulation depth of 99.6% for TE polarization and 98.9% for TM polarization were obtained.

Tunable mode converters with 500 strain induced SiO_2 grating pads of 1.5μm film thickness and 21μm spatial period were produced. More than 96% conversion efficiency for both TE and TM input was obtained. The -3dB optical bandwidth was 2.24nm and the suppression of the input polarization at phase-matched wavelength was more than 11dB for both TE and TM polarization.

A two-port polarization-independent electro-optically wavelength tunable filter has been fabricated based on the above results. The center wavelength of the filter is 1531nm at room temperature and the -3dB bandwidth is 2.4nm. The nearest side lobe is 13dB down relative to the main peak. A thermal tuning rate of –0.765nm/°C is achieved by changing the substrate temperature from 23°C to 11.5°C. Electrical tuning of the filter peak wavelength is demonstrated by applying DC voltage across electrodes with a gap of 17μm. A maximum tuning range of 12.8nm is obtained by changing the tuning voltage from -80V to +80V, indicating an electrical tuning rate of 0.08nm/V.

REFERENCES

1. Govind P. Agrawal, *Fiber Optic Communication Systems,* 2nd edition. New York: John Wiley & Sons, 1997.
2. H. Kobrinski and K. Cheung, "Wavelength-tunable optical filters: Applications and technologies," *IEEE Communications Magazine*, pp. 53-63, Oct. 1989.
3. H. F. Taylor and O. Eknoyan, "Guided wave acousto-optic and electro-optic tunable filter designs with relaxed beam-splitter requirements," *Applied Optics*, vol. 39, pp.124-128, Jan. 2000.
4. W. Warzanskyj, F. Heismann, and R. C. Alferness, "Polarization-independent electro-optically tunable narrow-band wavelength filter," *Applied Physics Letters*, vol. 53, pp. 13-15, Jul. 1988.
5. P. E. Green, Jr., *Fiber Optic Networks*. Englewood Cliffs, NJ: Prentice Hall, 1993.
6. D. K. Cheng, *Fundamentals of Engineering Electromagnetics*. Upper Saddle River, NJ: Prentice Hall, 1993.
7. Amnon Yariv, *Quantum Electronics*, 3rd edition. New York: John Wiley & Sons, 1989.
8. T. E. Murphy, "Integrated optical grating-based matched filters for fiber-optic communications," MS Thesis. Massachusetts Institute of Technology, Cambridge, MA, 1996.

9. Amnon Yariv, *Quantum Electronics*, 3rd edition. New York: John Wiley & Sons, 1989.

10. Theodor Tamir, *Guided-Wave Optoelectronics*. Berlin Heidelberg: Spring-Verlag, 1988.

11. H. Nishihara, M. Haruna, and T. Suhara, *Optical Integrated Circuits*. New York: McGraw-Hill, 1989.

12. D. F. Nelson and R. M. Mikulyak, "Refractive indices of congruently melting lithium niobate," *Journal of Applied Physics*, vol. 45, pp. 3688-3689, Aug. 1974.

13. Z. Tang, "Study of utilizing static photoelastic effect in integrated optical devices," Ph.D. Dissertation, Texas A&M University, Department of Electrical Engineering, College Station, Texas, 1994.

14. Personal communications with O. Eknoyan, Texas A&M University, Dept. of Electrical Engineering, College Station, Texas, 2003.

15. W. K. Burns, T. G. Giallorenzi, R. P. Moeller, and E. J. West, "Interferometric waveguide modulator with polarization-independent operation," *Applied Physics Letters*, vol. 33, pp. 944-947, Dec. 1978.

16. R. C. Alferness and L. L. Buhl, "Electro-optic waveguide TE↔TM mode converter with low drive voltage," *Optics Letters*, vol. 5, pp 473-475, Nov. 1980.

17. J. L. Jackel, V. Ramaswamy, and S. P. Lyman, “Elimination of out-diffused surface guiding in titanium-diffused $LiNbO_3$,” *Applied Physics Letters,* vol. 38, pp. 509-511, Apr. 1981.

18. R. J. Holmes and D. M. Smyth, “Titanium diffusion into $LiNbO_3$ as a function of stoichiometry,” *Journal of Applied Physics,* vol. 55, pp. 3531-3535, May 1984.

19. E. L. Wooten, et al., “A review of lithium niobate modulators for fiber-optic communications systems,” *IEEE Journal of Selected Topics in Quantum Electronics,* vol. 6, pp. 69-82, Jan./Feb. 2000.

20. P. Tang, “Polarization independent electrooptically tunable add drop filter in Ti:$LiNbO_3$ at 1.55μm wavelength regime,” Ph.D. Dissertation, Texas A&M University, Department of Electrical Engineering, College Station, Texas, 2002.

21. R. C. Alferness and L. L. Buhl, “Long-wavelength Ti:$LiNbO_3$ waveguide electro-optic TE↔TM converter,” *Electronics Letters,* vol. 19, pp. 40-41, Jan. 1983.

22. R. C. Alferness and L. L. Buhl, “Tunable electro-optic waveguide TE↔TM converter/wavelength filter,” *Applied Physics Letters,* vol. 40, pp. 861-862, May 1982.

23. F. Heismann and L. L. Buhl, “Electro-optically tunable narrowband Ti:$LiNbO_3$ wavelength filter,” *Electronics Letters,* vol. 23, pp. 572-574, May 1987.

APPENDIX 1

FABRICATION PROCEDURE OF TUNABLE WAVELENGTH FILTER

- Dicing $LiNbO_3$ substrate (X-cut, Y-propagation).
- Clean samples with proper solvents.
- Deposit Ti film by DC Sputtering.
- Delineate waveguide pattern by positive photolithography process.
- Vacuum hard bake the photoresist and O_2 descum.
- Dry etch Ti film using reactive ion etching (RIE).
- Wet etch to remove residual Ti using diluted HF acid.
- Diffuse delineated Ti pattern.
- Polish end edges.
- Pattern electrodes using image reversal photolithography.
- Deposit metal films with E-Beam and delineate electrodes pattern by liftoff.
- Deposit SiO_2 using E-Beam system with substrate maintained at elevated temperature (360°C).
- Delineate grating pattern by positive photolithography, hard bake the photoresist, etch unwanted SiO_2 in RIE system, and remove any remaining residual film in buffer oxide etch.

APPENDIX 2

CUTTING A SUBSTRATE WITH THE DICING SAW

- Mount blue tape and stick $LiNbO_3$ wafer on the tape.
- Turn on 4 knobs/switches for saw: air knob under bench (by heater &oil polisher, black); vacuum pump power switch under saw (silver); vacuum line switch (black, flip up); water line valve under saw (yellow)
- MEASURE RESISTANCE BETWEEN BLADE AND SPINDLE! Should be less than 1 or 2 kΩ (use lowest reading).
- **R** Turn on saw power (big red button).
- Select program button and check parameters, program 300 is used.
- Mode 30, speed=0.127 mm/s, 25000 rpm.
- For 1mm thick wafer, Height = 0.6 mm, Thickness=1.2mm.
- **R** Turn spindle on.
- Zero chuck (be prepared to press RESET if blade cuts into chuck).
- **R** Vapor lock wafer onto platform.
- Press ALIGN, align stage/sample with crosshairs using panel on right.
- Make a test cut on tape but not on the sample (to cut -- press SINGLE CUT).
- Align the substrate with cross hairs and cut.
- When finished, do steps marked R in reverse order to shut down system.

APPENDIX 3

SUBSTRATE CLEANING PROCEDURE

- Brush with a Q-tip using soapy water.
- Rinse thoroughly with D.I. water.
- Sonicate in Acetone for 10 minutes.
- Rinse with Methanol.
- Sonicate in Methanol for 10 minutes.
- Rinse with D.I. water.
- Sonicate in soap water for 10 minutes.
- Rinse with D.I. water.
- Sonicate in D.I. water for 10 minutes.
- Brush gently with a Q-tip using Methanol.
- Blow dry with N_2.

APPENDIX 4

DC SPUTTERING PROCESS

- Vent the bell jar and load sample(s).
- Close bell jar and turn on mechanical pump on the back.
- Turn on ‘Chamber Roughing Valve’ and wait until roughing pressure below 50μm.
- Close Chamber Roughing Valve and open high vacuum valve all the way.
- Wait about 2 hours until the pressure is below $3x10^{-6}$ Torr.
- Turn on the cooler for thickness monitor and set temperature @ 10 ˚C.
- Ar gas flow rate @ 140 sccm.
- Adjust high vacuum valve to make Hastings vacuum gauge @ 20 μm.
- Set thickness monitor.
- Turn on power supply and push the red button, turn dial slowly (to right).
- Sputtering condition (current: 40 mA).
- 15 minutes pre-sputtering (check current frequently)
- Start deposition by adjusting sample position.
- After finishing deposition, turn dial left, turn off power supply.
- Close LEAK valve and turn off Ar gas flow switches, close Ar gas duel.
- Set the temperature for the cooler @ 25 ˚C and wait until temperature is stable.
- Wait for more than 2 hours before taking out sample.

APPENDIX 5

POSITIVE PHOTOLITHOGRAPHY PROCESS

- Dehydrate sample @ 135°C for 5 minutes.
- Let sample cool for 10 minutes.
- Spin AZ5214 photoresist for 30 sec @ 5000 rpm.
- Soft bake sample for 2 minutes @ 100°C.
- Let sample cool for 10 minutes.
- Expose UV with mask for 8 seconds @ 17mW/cm^2 with filter.
- Develop in MF312:H_2O (1:1.2) solution for about 45 seconds.
- Thoroughly rinse sample in water.
- Soft blow dry with Nitrogen.

APPENDIX 6

O_2 PLASMA ASHING

- Vent and load sample into barrel asher.
- Pump chamber and O_2 line down to a pressure of 50 μm.
- Establish O_2 flow so that the chamber pressure is 500 μm.
- Turn on forward RF power to 100 watts.
- Tune RF system so that reflected power is less than 5 watts.
- Run RF for 5 minutes.
- Turn off power. Vent and take out sample.

APPENDIX 7

REACTIVE ION ETCH (RIE)

- Turn on the main power.
- Vent and load sample(s).
- Turn on mechanical pump.
- Open soft roughing line till pressure drops below 7000μm.
- Close soft roughing line, open high vacuum valve, turn on blower
- Wait until pressure drops below 20μm, turn throttle valve to auto.
- Wait until the pressure stabilizes at 70μm, then turn on the gases:

  Gas flow rate (reading): CHF_3 ~ 30sccm, Ar ~ 3sccm, He ~ 7.5sccm.
- Wait until the flows stabilize, turn on RF power, adjust forward power to 350W, tune reflected power to 0, and start etching.
- After finishing etching, turn off RF power, close gases, turn throttle valve to open, wait 2 minutes.
- Close high vacuum valve, turn off Baratron and blower, vent chamber, take out samples.

APPENDIX 8

TITANIUM IN-DIFFUSION PROCESS

- Load cleaned sample onto alumina (Al_2O_3) sample holder, and put sample holder in the center of alumina tube.
- Use glass rod to push alumina tube to the center of quartz tube.
- Seal tube with quartz cap at front and connect to bubbler.
- Turn on compressed air and adjust airflow at the back of furnace.
- Adjust settings for desired temperature.
- Wait until the airflow stabilizes at 1 bubble/sec and then turn on control switch.
- Wait until current meter stabilizes then turn on element switch.
- It takes about 45 minutes for furnace to heat over 1000°C.
- When current meter starts to swing on/off, begin counting diffusion time.
- Maintain bubbling rate at 1 bubble/second at front during the process
- After completion of the diffusion, turn off element and control switch.
- After temperature drops below 200°C, close gas and open the front end by removing the quartz cap.
- After furnace fully cools down, take out alumina tube and the sample.

APPENDIX 9

POLISHING PROCESS

Mounting

- Apply one small drop of UV epoxy (Norland optical adhesive P/N 8101) to the waveguide surface of one sample.
- Place a second sample upside-down on top of the first sample so that the waveguide surfaces are together.
- Secure samples into polishing mount so that they protrude 2-3 millimeters.
- Expose under ultra-violet light for 10 minutes at each end to cure epoxy.

Rough polish

- Secure mount to polishing fixture.
- Mix 0.5 teaspoon of polishing grit with lapping oil and spread mixture evenly over the rough polishing plate.
- Polish at speed 6 RPM for approximately 10-15 minutes (just enough to plane the surface).
- Unfasten mounting fixture from polishing fixture and clean.

Fine polishing

- Mix 3 μm diamond polishing grit with water, soap and suspendex following recipe for proportions.

- Pour onto polishing wheel and into polishing tray.
- Put polishing jig onto the plate.
- Turn on pump to circulate slurry mixture.
- Polish for 60 minutes at 16 rpm.
- Clean all equipment thoroughly.
- Repeat fine polishing procedure with 0.3 μm diamond polishing grit.
- Polish for 45 minutes at 16 rpm.

Dissolve epoxy

- Soak sample in MF312 until it separates.
- Rinse thoroughly with water.
- Inspect edges quality and cleanness under microscope before optical testing.

APPENDIX 10

IMAGE REVERSAL PHOTOLITHOGRAPHY PROCESS

- Dehydrate (in 135°C oven) for 5 min, wait 10 min for samples to cool down.
- Spin at 5000rpm for 30 sec.
- Pre soft bake at 90°C (setting 105°C) for 1 min.
- Fast exposure for 0.8 sec (with Mask, without Filter, 10.6 mw/cm^2).
- 2^{nd} softbake at 105°C (setting 120°C) for 2 min (for reversal).
- Flood exposure for 2 min (without mask, without Filter, 10.6 mw/cm^2).
- Develop ~28 sec (MF312:DI H_2O =1:1.2).
- Thoroughly rinse sample in DI water, and gently blow-dry with Nitrogen.

APPENDIX 11

E-BEAM PROCEDURE

Check Thickness Monitor

- Turn on thickness monitor. The light should flash twice. If it keeps flashing, there is something wrong with the thickness monitor.

Vent the system

- Flip on the control and make sure roughing valve and Hi-vacuum valve are closed.
- Open the N_2 gas tank; turn on the vent switch and open the valve in the back.

Load samples

Pump down system

- Close the lid.
- Turn on the mechanical pump and open roughing valve. Pump until pressure <70μm.
- Close the roughing valve. Open Hi-vacuum valve in the back.
- Pump until the system pressure is less than $5x10^{-6}$ torr.

(To heat substrate only)

- Turn on variac (to ~80v for 360°C) when pressure below 1×10^{-5} torr.

Set the thickness monitor

- Turn power on.
- Set the keyboard switch to Program. Set Control PWR to Auto.

- Set density, Z-ratio and tooling.
- Reset Keyboard switch to Lock and reset Control PWR to Main Power.
- Press ZERO button.

Deposition

- Open cooling water.
- For hot SiO_2, open O_2 bottle and valve by the chamber slowly and adjust flow rate (with knob by the valve) to make system pressure ~3×10^{-5} torr (about 1sccm flow).
- Plug in the key at the back.
- Plug in main power for power supply.
- Turn on the main power switch, and wait for system to start.
- Press the High Voltage On button and wait for relay sound.
- **CAUTION:** *If current shows, turn off High Voltage immediately. Short circuit is presented.*
- Turn on the scanner.
- Wait for the beam to warm up.
- Increase the current gradually and adjust the light spot position.
- After finish, turn down the current and voltage. Plug off the key
- Rotate the crucible if you're using more than one and repeat (be sure to plug off the main power while rotating)
- Turn off the ionization gauge

- For hot SiO_2, open O_2 flow rate valve all the way. Let O_2 flow on until sample cools down below 50 °C.
- Wait for 5 min and turn off the power supply
- Wait for 15 min, close cooling water for crystal and turn off crystal cooler.
- Wait for 45 minutes and close other cooling water under the front panel.
- Close Hi vacuum (Gate switch).
- Turn off control.

APPENDIX 12

MASK LAYOUT FOR INTERFEROMETER WAVEGUIDES

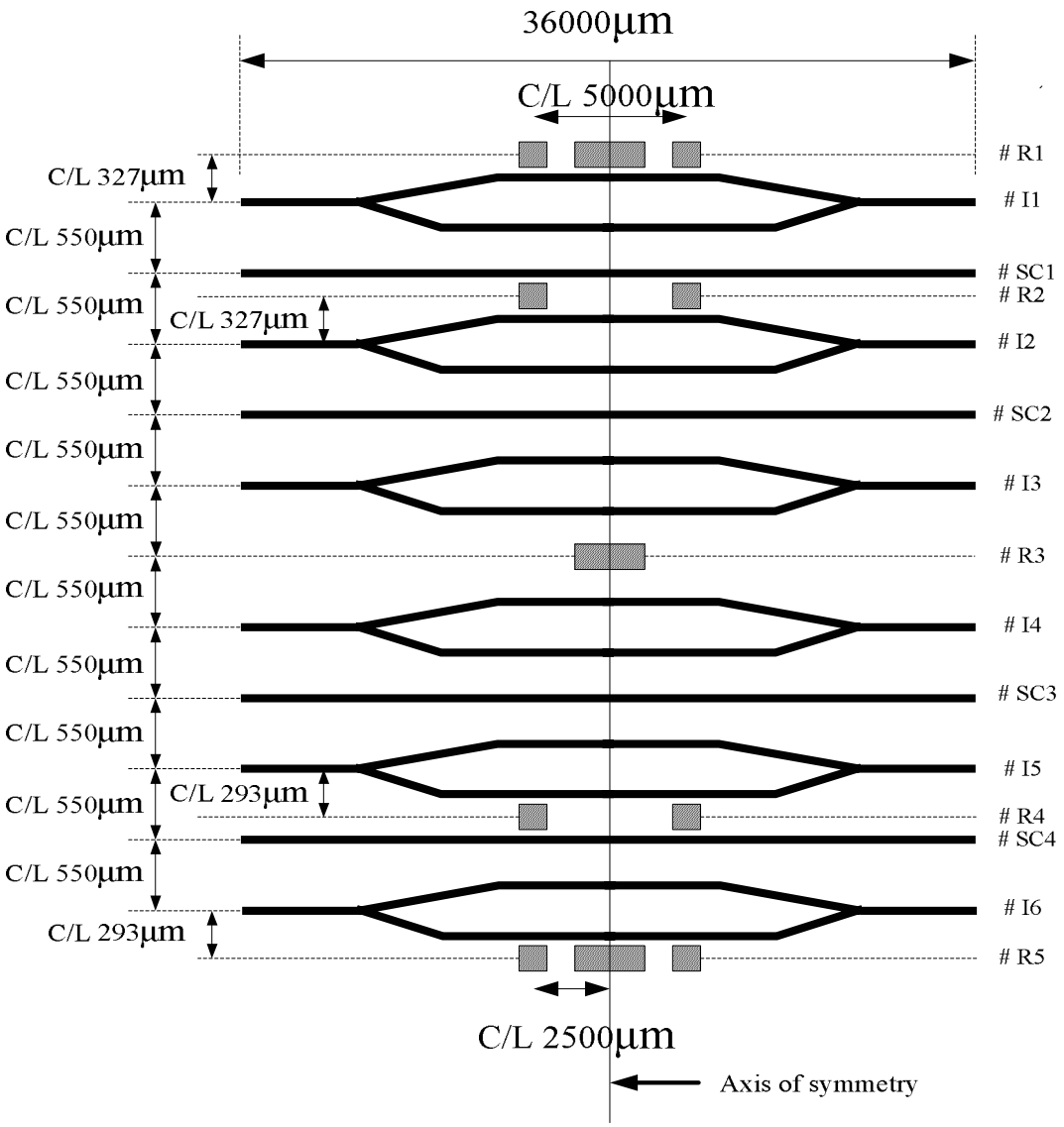

R=References for alignment and film thickness marks I=Interferometers SC=Strait Channel W/G C/L=Center Line

Fig. 29. Mask layout for interferometer waveguides.

APPENDIX 13

DETAILS FOR INTERFEROMETER

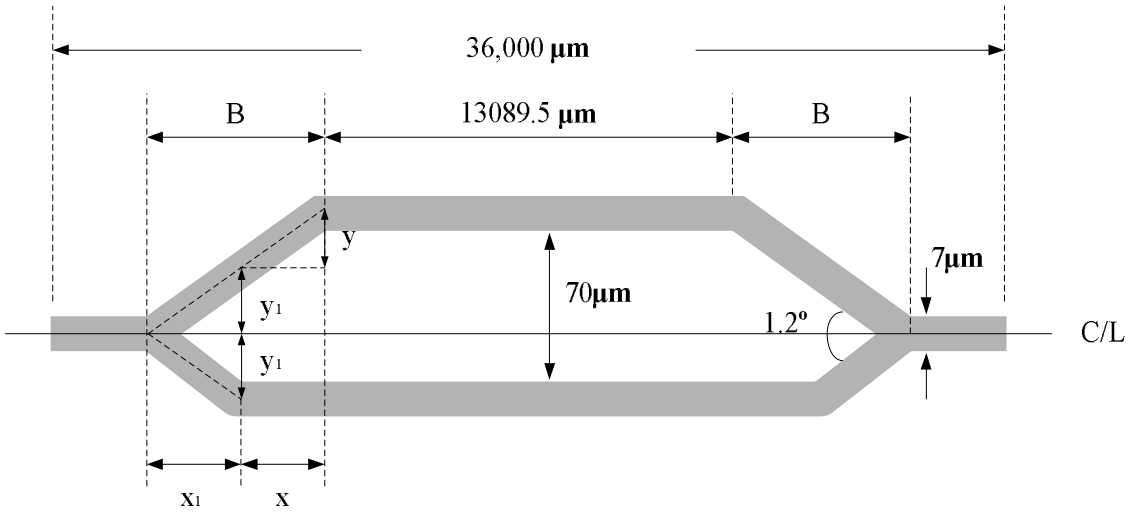

Note: Dimension x_1, y_1, x, y and B refer to enter dashed lines which are the axes of waveguides.

Fig. 30. Detailed configuration of interferometers.

Table 6. Detailed dimension of interferometers.

Device #	**I1**	**I2**	**I3**	**I4**	**I5**	**I6**
x_1 [µm]	2056.03	2056.03	2073.44	2051.56	2051.56	2069.11
y_1 [µm]	21.53	21.53	21.71	21.48	21.48	21.67
x [µm]	3240.62	3240.62	3205.82	3249.57	3249.57	3214.47
y [µm]	33.94	33.94	33.57	34.03	34.03	33.66
B [µm]	5296.66	5296.66	5279.25	5301.13	5301.13	5283.58

APPENDIX 14

GRATING PATTERN

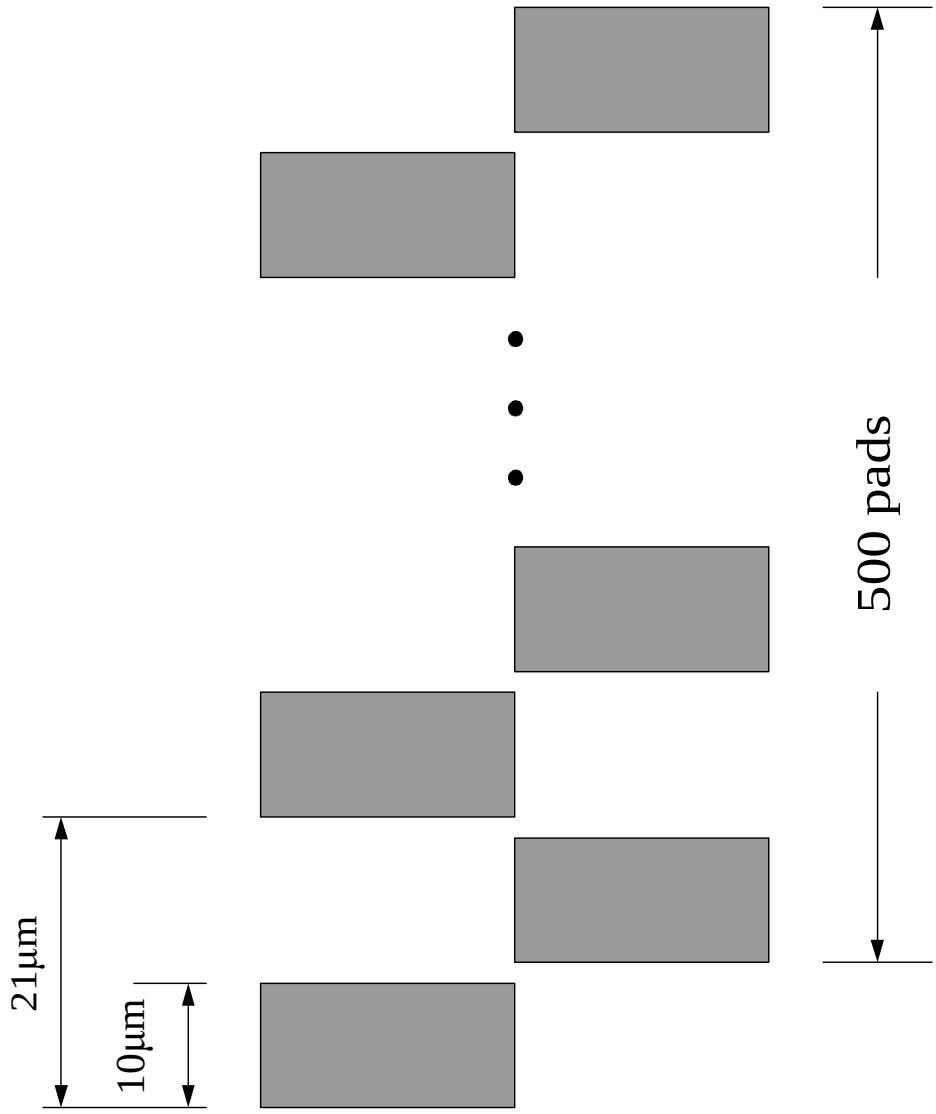

Fig. 31. Grating pattern.

VITA

Yang Ping was born in Hangzhou, Zhejiang Province, People's Republic of China. He received a B.S. in electronic engineering from Tsinghua University (P. R. China) in July 2000. Upon graduation, he attended Texas A&M University in August 2000 and received his M.S. degree in electrical engineering. He can be reached at the following address:

1 Hensel Dr, Apt. X2K

College Station, TX 77840